# Characterization of Three-Level Control in Capacitively-Shunted Flux Quantum Circuits Using Randomized Benchmarking

by

Michal Kononenko

A thesis
presented to the University of Waterloo
in fulfillment of the
thesis requirement for the degree of
Master of Science
in
Physics (Quantum Information)

Waterloo, Ontario, Canada, 2021

## Author's Declaration

This thesis consists of material all of which I authored or co-authored: see Statement of Contributions included in the thesis. This is a true copy of the thesis, including any required final revisions, as accepted by my examiners.

I understand that my thesis may be made electronically available to the public.

## Statement of Contributions

Michal Kononenko was the sole author for Chapters 1, 2, 4, and 5. These were written under the supervision of Adrian Lupascu, and were not written for publication.

Chapter 3 consists of co-authored content. Michal Kononenko was the lead author of the paper on which this chapter is based. Substantial contributions to and review of this paper were provided by Muhammet Ali Yurtalan and Adrian Lupascu. Muhammet Ali Yurtalan and Adrian Lupascu worked on the design and modeling of the device, as well as the experimental setup and device simulations. Muhammet Ali Yurtalan and Jiahao Shi fabricated the device on which the experiment was conducted. Michal Kononenko and Muhammet Ali Yurtalan conducted the experiments, and conducted the data analysis. Substantial contributions to the code used to run the experiments were provided by Michal Kononenko, Adrian Lupascu, and Muhammet Ali Yurtalan. Sahel Ashhab provided the model for calculating qubit level shifts, and reviewed the paper on which Chapter 3 is based. Adrian Lupascu supervised the experimental work. The work presented in Chapter 3 is based on [1].

In Chapter 4, the Mathematica simulation was first developed by Muhammet Ali Yurtalan, and then adapted by Michal Kononenko to evaluate the designs presented. Adrian Lupascu supervised the research, and provided guidance and code review.

## Abstract

Superconducting devices have emerged as leading candidates for building practical quantum computers, owing to their scalability, designability, and ease of control. Development of superconducting devices has been accompanied by increases in coherence times from nanoseconds to tens of microseconds, and a multitude of new types of superconducting qubits. In turn, these improvements in coherence, and study of superconducting qubits has produced models for these devices accurate and trustworthy enough to enable design decisions to be determined prior to device fabrication. Recent work by the superconducting quantum devices (SQD) group has produced a variant of the capacitively-shunted flux qubit that features fast control over the lowest three levels, allowing the device to be used as a qutrit. This thesis presents a model and characterization results for this device.

This thesis also presents experimental results characterizing control fidelity for a qutrit using randomized benchmarking (RB). Quantum process tomography and application of repeated gate sequences are also used to support the randomized benchmarking results. The method of synthesizing the gates in the qutrit Clifford group can decompose any gate into two-state rotations. The fidelity of $99.0 \pm 0.2\,\%$ obtained by randomized benchmarking establishes the device as a useful qutrit, and outlines interesting directions in using higher levels to improve qubit-based quantum computers, and in using higher levels to pack more states into fewer devices in quantum computers. Analysis of experimental results indicates errors are dominated by ac-Stark and Bloch-Siegert shifts during qutrit control.

This thesis then presents two new devices meant to study the impact of changing design parameters on the suitability of flux qubits for multilevel control. The first device tests individual qubits, with the goal of further improving the coherence time, and improving qutrit control. The second device couples two devices together, so that two-qubit gates can be studied. The available design parameters and their impact on qubit properties are discussed, and design variations are selected for the single and two-qubit devices. The result is a set of devices ready for manufacture and experimental characterization.

**Acknowledgements**

I would like to thank my supervisor Prof. Adrian Lupascu for his exemplary supervision of my research, for encouraging me during difficult times, and for helping me to appreciate the successes of this research. Without his exemplary skills in experiment methodology, dedication to experimental physics, discipline, and patience to see me through my faults, this research would be impossible.

I am thankful to Prof. Sahel Ashhab for reviewing the manuscript on which Chapter 3 is based. I am also thankful to Prof. Matteo Mariantoni for serving on my advisory and thesis committee, Prof. Crystal Senko for serving on my advisory committee, and Prof. Jonathan Baugh for serving on my thesis committee.

I would also like to thank Dr. Muhammet Ali Yurtalan for the hours of discussions, training and collaboration in setting up and running the experiments presented in Chapter 2 and 3. Dr. Yurtalan's tireless efforts in designing, fabricating, and controlling the three-pad flux qubit were essential to realizing this research successfully. I am also grateful to Muhammet Ali Yurtalan and Jiahao Shi for manufacturing the device, and to Jiahao Shi for training me in qubit fabrication.

I am also grateful to all the current and former members of the SQD research group, including Dr. Muhammet Ali Yurtalan, Jiahao Shi, Noah Cornelius Janzen, Shaun Ren, Xi Dai, Denis Melanson, Dr. Salil Bedkihal, and Dr. Mehmet Canturk. The many fruitful discussions, support, and ideas have been a profound influence on my research and the research presented in this thesis. I am humbled by the opportunity to work with such a group of dedicated researchers.

I thank the Quantum Nanofab, IQC IT support, and Roberto Romero for microfabrication, IT, and technical support in realizing the research presented in this thesis.

Lastly, I would like to thank my friends and family for their encouragement and support during my studies.

# Table of Contents

**List of Figures** viii

**List of Tables** xi

**1 Introduction** 1

1.1 Outline of Thesis . . . 2

**2 Introduction to Capacitively-Shunted Flux Qubits** 4

2.1 Superconducting Circuits . . . 4

2.2 Types of Superconducting Qubits . . . 7

2.2.1 Charge Qubits . . . 7

2.2.2 Flux Qubits . . . 8

2.3 Flux Qubit Control and Readout . . . 10

2.4 Sources of Decoherence . . . 12

2.5 Measuring CSFQ Properties . . . 13

2.6 Characterizing Gates on a CSFQ . . . 17

2.6.1 The Average Gate Fidelity . . . 17

2.6.2 Quantum Process Tomography . . . 19

2.6.3 Randomized Benchmarking . . . 19

**3 Qutrit Randomized Benchmarking** **22**

3.1 The Randomized Benchmarking Experiment . . . . . 22

3.2 Experiment Details . . . . . 31

3.3 The Gate Decomposition . . . . . 32

3.4 Numerical Simulation of Device Dynamics . . . . . 35

3.5 Calculation of Gate Fidelity . . . . . 36

3.6 Approximating the Fidelity of Clifford Gates from Givens Rotations . . . . 37

3.7 Effective Hamiltonian Calculation . . . . . 39

**4 Designing a New Generation of Capacitively-Shunted Flux Qubits** **40**

4.1 Introduction . . . . . 40

4.2 Designing Single CSFQ Devices . . . . . 41

4.3 Coupled CSFQ Devices . . . . . 50

4.4 Conclusions . . . . . 57

**5 Conclusions** **59**

**References** **61**

**APPENDICES** **68**

**A PDF Plots From Matlab** **69**

# List of Figures


2.1 A diagram of an LC oscillator driven by a current source . . . . . 5

2.2 (a) A circuit diagram of a charge qubit. (b) A micrograph of a transmon qubit, taken from Figure S1 of [2] , with capacitances from Figure 2.2 (a) labelled. . . . . 8

2.3 (a) A circuit diagram for the three-pad CSFQ, without any control or read-out lines connected. (b) A micrograph of the device, with circuit depicted . (c) The lowest seven energy levels of the device versus the applied external flux. $E = 0$ is referred to the energy of the ground state at the symmetry point. . . . . 9

2.4 (a) The transmission spectrum of the CSFQ device versus magnetic field biasing voltage. (b-d) Low power Transmission spectroscopy, showing $\langle V_h \rangle$ versus control frequency from (top to bottom), the 01 (b), 12 (c), and 02 (d) transitions. (e) The result of a typical Rabi experiment on 01, showing $\langle V \rangle$ versus the delay time $\tau$ (f) Rabi frequency versus voltage for the 01, 12, and 02-two photon transitions. (g) Rabi frequency versus drive voltage for the 02 two-photon transition. Note the quadratic dependence of Rabi frequency on drive voltage. . . . . 15

2.5 (a) A typical $T1$ experiment result, with $T_1 = 46.1 \pm 2.5\,\mu$s. (b) A typical Ramsey experiment result, with $T_2^* = 4.7 \pm 0.3\,\mu$s. (c) The multi-level relaxation result . . . . . 17

2.6 A result for qubit RB on the 01 space of the CSFQ. . . . . 21

3.1 A representation of the experiment setup. (a) A scanning electron micrograph of the device on which the experiment was performed, with connections to the control AWG and the readout setup shown. The control AWG is synthesizing a sequence of Clifford gates $C_1$ to $C_n$ for an RB experiment. (b) The waveform for a Walsh-Hadamard gate $H_3$ as outputted by the control AWG. Black (dark) lines indicate $|0\rangle - |1\rangle$ driven transitions and red (light) lines indicate $|1\rangle - |2\rangle$ driven transitions (c) A level diagram for the qutrit, with transition frequencies shown. . . . . 24

3.2 Experiment and simulated results for qutrit RB. (a) The experimentally-measured $\langle V \rangle$ compared to three simulation results. Simulation 1 is the numerically-simulated result. Simulation 2 is like Simulation 1, but with $V_3$ and $V_6$ optimized to match experiment data. Simulation 3 is like Simulation 1, but with decoherence modelled as well. Fits to equation 3.1 are shown for the experiment and each simulation. (b) The populations from Simulation 1 with the leakage analysis from [3] performed on them. The dashed line is an exponential fit for $P_0$ vs $l$. . . . . 26

3.3 $\langle V \rangle$ versus $N$ for repeated applications of $H3$, $X3$, $S3$, and $Z3$, shown in panels (a), (b), (c), and (d) respectively. The red circles are the expected $\langle V \rangle$ versus $N$ signal for the ideal gate, and the black squares are the experiment results. . . . . 27

3.4 (a) The error of the Clifford gate versus the sum of the errors of the component Givens rotations for $\mathcal{C}_3$ at various drive frequencies. The line of best fit and 95% prediction bands are also shown. (b) The error versus the drive frequency for a set of Givens rotations, at $\Omega = 2\pi \times 50$ MHz. The Stark shift and Bloch-Siegert Shift shown for (c) $R(\pi)_0^{01}$ and for (d) $R(\pi)_0^{12}$. The lines in (c) and (d) show quadratic fits. . . . . 30

3.5 The waveforms implementing the qutrit gates $H_3$ (a), $S_3$ (b), $X_3$ (c), and $Z_3$ (d). Black (dark) areas indicate 01 transitions and red (light) areas indicate 12 transitions. . . . . 34

3.6 The simulated error for each Clifford gate versus its (a) zeroth-order estimate and (b) first-order estimate. The line of best fit and 95% prediction bands are shown as well. . . . . 39

4.1 An illustration labelling the control antenna, control line, and readout resonator connections for a single qubit. The labelled dimension shows the 175 $\mu$m distance required to isolated the control line from the qubit . . . . 46

4.2 Plots of design parameters as a function of the critical current $I_c$ and $\alpha$. (a) The 01 transition frequency. (b) The 01-transition frequency with geometry scaled by 0.6. (c) The persistent current. (d) The 01 anharmonicity. (e) The difference betwen $\omega_{23}$ and $\omega_{12}$, and (f) the charge modulation. . . . . 48

4.3 Simulation results of (a) a 7.3 GHz half-wavelength resonator coupled to a feedline, and (b) the portion of the resonator from (a) coupling to the feedline, with the other end connected to a 50 Ω port. (c) The real and imaginary components of $S_{12}$ obtained from the resonator in (a), with a simultaneous fit of the components to the expected $S_{12}$. . . . . 49

4.4 A drawing showing the baseline variation for the single-CSFQ device. (a) The partitioning of a 4" wafer into chips, and the location of the $17 \times 17$ mm chip on the wafer. (b) The $17 \times 17$ mm chip partitioned into $7 \times 3$ mm dies, and the location of the baseline variation on this chip. (c) The baseline variation of the Josephson junction for (d) the single-qubit CSFQ design. Green arrows indicate the direction in scaling, from large features to small features. . . . . 51

4.5 A drawing of the coupled CSFQ device, with coupling capacitances indicated. Each label refers to a pad on the CSFQ device, with each pad on the left qubit $Q1$ capacitively coupled to each pad on $Q2$. . . . . 53

4.6 A drawing of the baseline variation of the coupled CSFQ device. The two qubits to be coupled are in the center of the device. Each qubit has a dedicated readout resonator, control line, and flux line. Test structures are placed on the chip to check junction critical current, and the quality of lithography. Alignment marks (blue and yellow structures) are placed in the corners to ensure dimensional alignment during lithography. . . . . 56

# List of Tables


3.1 The decoherence rates measured in the qutrit space. . . . . 32

3.2 The Givens Rotation decompositions for $H_3$, $S_3$, $X_3$, and $Z_3$. . . . . 33

3.3 The coefficients of $H_{\text{static}}$ used in simulations. All other coefficients not shown are zero. . . . . 35

3.4 The coefficients of $H_{\text{drive}}$ used in simulations. All other coefficients not shown are zero. . . . . 36

# Chapter 1

# Introduction

Quantum computers are computers that use quantum-mechanical effects to implement quantum algorithms [4]. For a large class of problems, including integer factorization (Shor's algorithm) [5, Sec. 5.3.1], unstructured search (Grover's algorithm) [5, Ch. 6], and simulation of quantum systems, quantum algorithms achieve answers in significantly fewer operations than equivalent classical algorithms. See [5, Sec. 6.1] for an example. In the gate model of quantum computing, the quantum algorithm is encoded into a sequence of operations called gates, which map a space of quantum states to another space of states. These gates are applied to a known initial state, and measurement of this state after gate application yields the solution. Randomized benchmarking (RB) is a class of protocols that can efficiently measure how well a quantum computer implements a quantum gate set [6].

A qubit is a quantum system with two orthogonal states $|0\rangle$ and $|1\rangle$ which can be prepared in a known state, controlled, and measured [5, Ch. 7]. Qubits are the building blocks of quantum computers. In recent years, superconducting qubits have emerged as a candidate platform for quantum computing, owing to their ease of control and measurement and scalability to multi-qubit systems [7]. Interest in superconducting quantum computing has grown due to improved understanding of decoherence in superconducting devices, and development of new qubit designs that are less sensitive to noise channels that cause decoherence [8, Ch. 1]. These types of superconducting qubit can store quantum information for longer periods while retaining fast control present in earlier devices, meaning more quantum gates can be carried out before the qubit decoheres. The flux qubit, also known as the persistent current qubit [9], consists of three superconductor-insulator-superconductor junctions, also known as Josephson junctions, arranged in a loop. This type of qubit features a $|0\rangle$ and $|1\rangle$ state that are well isolated from other excitations in the qubit, fast

control, and a relatively long coherence time, making it a good candidate for building quantum computers.

Recent work in the superconducting quantum devices (SQD) group, including [10] and [11], has led to a flux qubit with gate times on the order of nanoseconds, and coherence times on the order of microseconds. In addition, control has been demonstrated on qubits encoded using the ground ($|0\rangle$) and first excited state ($|1\rangle$), as well as qubits encoded using the first excited and second excited state $|2\rangle$. This opens up the possibility of using the device presented in [10] as a base-three qubit, known as a qutrit. With more states available per device, larger quantum computers can be built with fewer devices. The device was shown to be excellent for qutrit control, but the procedure was not checked efficiently, and two-qubit gates between devices of this type were not demonstrated. This thesis presents a qutrit RB experiment that demonstrates qutrit control, and presents a set of devices to further understand the flux qubit, and to study two-qubits gates using flux qubits.

## 1.1 Outline of Thesis

Chapter 2 introduces the elements of superconducting circuits required to understand a capacitively-shunted flux qubit (CSFQ). Next, it discusses how to experimentally determine the CSFQ properties. Finally, the chapter introduces randomized benchmarking as a tool for characterizing a gate set on the CSFQ. Each property is also related to experimental results.

Chapter 3 discusses the qutrit randomized benchmarking experiment. It shows how to decompose arbitrary qutrit gates into two-level rotations, and how to build up those rotations into a randomized benchmarking sequence. The average fidelity of $99.0 \pm 0.2\,\%$ over the elements of the qutrit Clifford group was compared to quantum process tomography (QPT) on a subset of the Clifford group. Errors are dominated by ac-Stark and Bloch-Siegert shifts. This experiment demonstrates that high-fidelity qutrit control can be achieved in flux qubits, and outlines new avenues for future work in superconducting qutrit control. Of particular interest is the need to correct for level shifts on transitions, even if those transitions are not being driven at a given time in the RB sequence.

Chapter 4 discusses a new generation of CSFQ devices to further qutrit control. These devices also study how well the CSFQ device implements two qubit gates, knowledge of which is necessary in order to use the CSFQ in quantum computers. The chapter begins by identifying the design attributes against which qubits are evaluated, followed by the design

parameters that can be altered to change the attributes. A set of single-CSFQ devices are then designed to study the effect of changing design parameters on CSFQ performance. Finally, a design for a two-qubit CSFQ device is presented.

Conclusions from the qutrit RB experiment and the design study are presented and discussed in Chapter 5.

# Chapter 2

# Introduction to Capacitively-Shunted Flux Qubits

## 2.1 Superconducting Circuits

Superconductivity is transport of charge without resistance. Superconductivity in aluminum is described by the Bardeen-Cooper-Schrieffer (BCS) theory [12]. This theory features electrons and phonons pairing into Cooper pairs, with Cooper pairs occupying a single quantum state with a single phase [13, Ch. 4]. This macroscopic occupation of a single quantum state is what enables superconductors to perform quantum computing. As a consequence of superconductivity, the magnetic flux $\Phi$ through a loop of superconductor must be an integer multiple of the flux quantum $\Phi_0$, given by

$$\Phi_0 = \frac{h}{2e}. \tag{2.1}$$

One can construct superconducting circuit elements analogous to classical circuit elements, such as capacitors and inductors [14], and so build superconducting circuits. In these circuits, the charge $Q$, voltage $V$ the current $I$, and the flux $\Phi$ are generalized to operators, as opposed to classical dynamical variables seen in conventional circuits [15, Sec. 3.1.1]. Current is the time derivative of charge, and voltage is the time derivative of flux. Ideal circuit elements, like capacitors and inductors, relate these variables to each other.

The capacitor relates current and flux via

$$I = C\ddot{\Phi}, \tag{2.2}$$

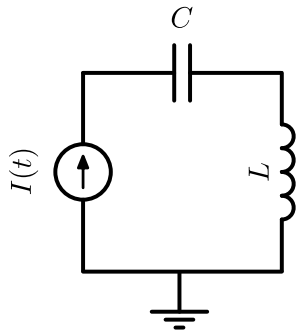


Figure 2.1: A diagram of an LC oscillator driven by a current source

where $C$ is the capacitance, and $\ddot{\Phi}$ is the second-order time derivative of $\Phi$. If $I$ and $\ddot{\Phi}$ are real numbers instead of operators, the classical capacitor relation is recovered. The inductor relates current and flux through

$$I = \frac{1}{L}\Phi, \tag{2.3}$$

where $L$ is the inductance.

The Josephson junction (JJ) is a circuit element unique to superconducting circuits, which behaves like a nonlinear inductor [15, Sec. 4.1]. Its current-flux relation is

$$I = I_c \sin\left(2\pi\frac{\Phi}{\Phi_0}\right), \tag{2.4}$$

where $I_c$ is the critical current of the junction [13, sec. 1.1.1].

The equations of motion for a superconducting circuit can be constructed and solved in a similar way to Kirchoff's laws for classical circuits [15]. For example, connecting an inductor in series with a capacitor and a time-dependent current source $I(t)$, as shown in Figure 2.1 gives the LC oscillator. From Kirchoff's flux law, the capacitor flux $\Phi_c$ and inductor flux $\Phi_l$ are equal to the flux from the current source $\Phi$. From conservation of current, the circuit equation of motion

$$C\ddot{\Phi} + \frac{1}{L}\Phi + I(t) = 0 \tag{2.5}$$

is obtained. This equation is equivalent to the equation of motion as a forced simple harmonic oscillator. Circuits made of inductors, capacitors, and Josephson junctions are

examples of Lagrangian systems. Their equations of motion are the solution of the Euler-Lagrange (EL) equations for an appropriately-formulated Lagrangian $\mathcal{L}$ [15, Sec. 2.1.8]. For a circuit with $n$ degrees of freedom given by $\Phi_1$ to $\Phi_n$, $\mathcal{L}$ is a function of the degrees of freedom, their derivatives, and the time. The EL equations are

$$\frac{d}{dt}\left(\frac{\partial \mathcal{L}}{\partial \dot{\Phi}_n}\right) - \frac{\partial \mathcal{L}}{\partial \Phi_n} = 0. \tag{2.6}$$

The charges $Q_n$ are the conjugate momenta to fluxes $\Phi_n$, given by

$$Q_n = \frac{\partial \mathcal{L}}{\partial \dot{\Phi}_n}. \tag{2.7}$$

For constraints of the type

$$f(\Phi_1, \Phi_2, ...\Phi_n) = 0, \tag{2.8}$$

such as flux quantization, one can solve the EL equations with one $\Phi_n$ written as a function of the others, and substituted into $\mathcal{L}$. In considering circuits with multiple and coupled capacitances and mutual inductances, and Josephson junctions, one can construct a general Lagrangian of the type

$$\mathcal{L} = \frac{1}{2}C_{ij}\dot{\Phi}_i\dot{\Phi}_j + \frac{1}{2}L_{ij}^{-1}\Phi_i\Phi_j + \Phi_0 I_{c,n}\cos\left(\frac{\Phi_n}{\Phi_0}\right), \tag{2.9}$$

with capacitance and inductance matrices $C_{ij}$ and $L_{ij}$. Equation 2.9 is specified together with the constraints. It is convenient to define $\gamma = 2\pi\frac{\Phi}{\Phi_0}$, at which point the Lagrangian becomes

$$\mathcal{L} = \frac{\Phi_0^2}{2}C_{ij}\dot{\gamma}_i\dot{\gamma}_j + \frac{\Phi_0^2}{2}L_{ij}^{-1}\gamma_i\gamma_j + \Phi_0 I_{c,n}\cos\gamma_n. \tag{2.10}$$

Time-dependent voltage and current controls are introduced by adding terms into the Lagrangian coupling a voltage (current) signal $V(t)$ ($I(t)$) to $\dot{\Phi}$ ($\Phi$) via $V(t)C_i\dot{\Phi}_i$ ($I(t)M_i\Phi_i$). After their introduction, it must be checked that $\mathcal{L}$ still produces the correct equation of motion. $C_i$ and $M_i$ represent the coupling capacitance and mutual inductance.

Every variable $\gamma_n$ has an associated generalized momentum given by

$$p_n = \frac{\partial \mathcal{L}}{\partial \dot{\gamma}_n}. \tag{2.11}$$

Taking the Legendre transform of $\mathcal{L}$ with respect to all the $p_n$ gives the Hamiltonian $H$, given by

$$H = \sum_n \dot{\gamma}_n p_n - \mathcal{L}. \tag{2.12}$$

Therefore, the Hamiltonian associated with the Lagrangian in equation 2.10 is

$$H = \frac{1}{2\Phi_0^2} C_{ij}^{-1} p_i p_j - \frac{\Phi_0^2}{2} L_{ij}^{-1} \gamma_i \gamma_j - \Phi_0 I_{c,n} \cos \gamma_n. \tag{2.13}$$

This circuit Hamiltonian can be quantized using canonical quantization by promoting $p_n$ and $\gamma_n$ to operators and imposing the canonical commutation relation $[\gamma_n, p_m] = i\hbar\delta_{mn}$ [14, Sec. 4]. The resulting Hamiltonian can be diagonalized, and its spectrum determines the energy levels of the circuit.

## 2.2 Types of Superconducting Qubits

This section specializes Section 2.1 to charge qubits and flux qubits, showing how to develop the Hamiltonian for both types of qubits.

### 2.2.1 Charge Qubits

The charge qubit, also known as the Cooper Pair Box (CPB), was the first superconducting device on which coherent control was performed [16]. It is composed of a capacitor in parallel with a JJ, and a gate capacitance connected to a voltage source. Figure 2.2 (b) shows an illustration of the CPB used in [2]. There is a single degree of freedom in the system, and $L_{ij}$ is negligible.

From the Hamiltonian in equation 2.13, $p$ can be associated with a charge $n$ through $p = \hbar n$. Defining the capacitance energy $E_C = \frac{\hbar^2}{2\phi_0^2(C+C_g)}$ and the Josephson energy $E_J = \phi_0 I_c$ gives the Hamiltonian

$$H = E_C \left( n + \frac{1}{2e} C_g V(t) \right)^2 - E_J \cos \gamma. \tag{2.14}$$

Writing out $\cos\gamma$ in the basis of $n$ allows the Hamiltonian to be written in the basis of the charge operator $\{|n\rangle\}$ [17, Sec. 1.2] as

$$H = E_C \sum_{n=0}^{\infty} n \left( n + \frac{C_g}{e} V(t) \right) |n\rangle\langle n| - E_J \sum_{n=-\infty}^{\infty} \frac{1}{2} \left( |n-1\rangle\langle n| + |n+1\rangle\langle n| \right) + \ldots$$
$$\ldots E_C \left( \frac{1}{2e} C_g V(t) \right)^2. \tag{2.15}$$

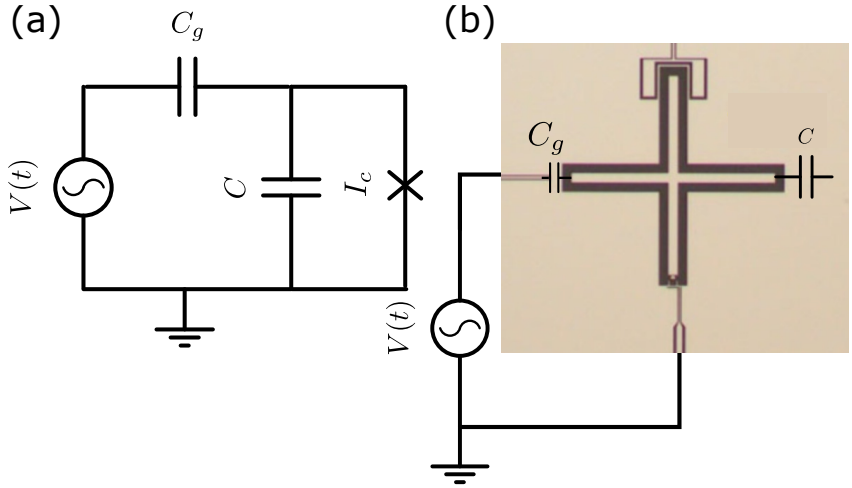


Figure 2.2: (a) A circuit diagram of a charge qubit. (b) A micrograph of a transmon qubit, taken from Figure S1 of [2] , with capacitances from Figure 2.2 (a) labelled.

In equation 2.15, $n$ refers to the eigenvalues of the number operator. The last term in equation 2.15 can be omitted as it is proportional to the identity operator. After truncating the infinite sums, $H$ can be diagonalized numerically. The ground state $|0\rangle$ and the first excited state $|1\rangle$ of $H$ are the states on which quantum computing can be performed.

By modifying $E_C$ and $E_J$, one can engineer the CPB to have desired parameters such as the transition frequency between $|0\rangle$ and $|1\rangle$. $E_C$ and $E_J$ can be set by different $C$ and $I_c$, which are in turn set by the qubit geometry. By designing for different $E_C$ and $E_J$, one can also design around possible problems in the circuit. For example, suppose $V(t)$ includes some noise in addition to the control signal. By placing a large capacitance in series with the junction, one can make the qubit less sensitive to voltage noise. This is the principle behind the transmon qubit [18]. However, the cost of this large shunt capacitance is that the qubit behaves more like a harmonic oscillator, making the qubit harder to control. Design decisions like these are crucial to designing good qubits. Chapter 4 describes such a design process for flux qubits.

### 2.2.2 Flux Qubits

The flux qubit, also called the persistent current qubit, consists of three Josephson junctions in series around a loop. [9]. Figure 2.3 (a) shows a circuit model for the flux qubit. There are three independent fluxes $\Phi_{21}$, $\Phi_{31}$, and $\Phi_{10}$, since $\Phi_{23}$ is set by flux quantization. Using

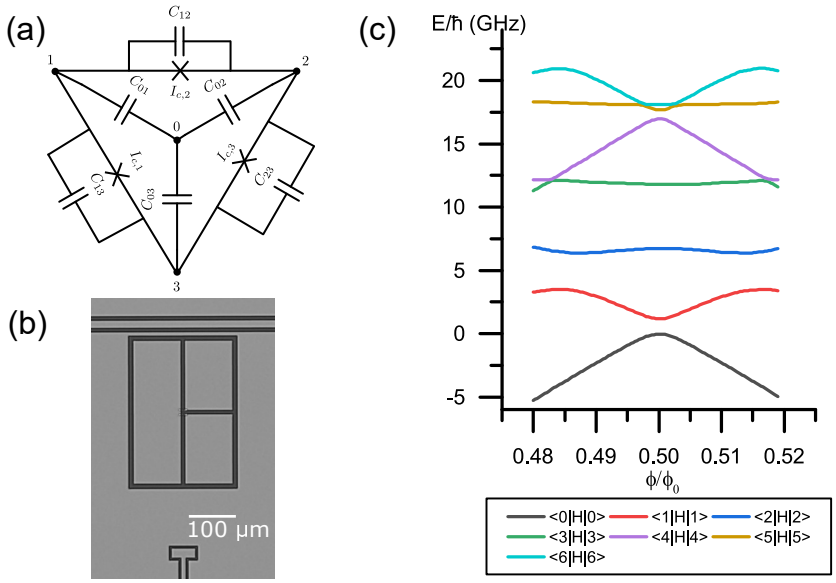


Figure 2.3: (a) A circuit diagram for the three-pad CSFQ, without any control or readout lines connected. (b) A micrograph of the device, with circuit depicted . (c) The lowest seven energy levels of the device versus the applied external flux. $E = 0$ is referred to the energy of the ground state at the symmetry point.

the circuit Hamiltonian 2.13 in the basis $(\gamma_{21}, \gamma_{31}, \gamma_{10})$, $C_{ij}$ is

$$C_{ij} = \begin{pmatrix} C_{12} + C_{23} + C_{02} & -C_{23} & C_{02} \\ -C_{23} & C_{13} + C_{23} + C_{03} & C_{03} \\ C_{02} & C_{03} & C_{01} + C_{02} + C_{01} \end{pmatrix}, \tag{2.16}$$

where the capacitances are referred to those in figure 2.3. The capacitances $C_{0i}$ refer to capacitances to the ground plane surrounding the CSFQ. The coupling capacitances are provided by the large capacitive pads shown in Figure 2.3 (b), on which the three Josephson junctions are placed.

If one of the three Josephson junctions is made smaller than the others by a factor $\alpha$, the transition frequencies can be tuned by an external magnetic flux $\phi_{ext}$ threading the Josephson junction loop [9]. This is shown in the energy level diagram of the lowest seven levels in Figure 2.3 (c). Note the large difference between the $|0\rangle \rightarrow |1\rangle$ and $|1\rangle \rightarrow |2\rangle$ transition, where $|2\rangle$ is the second excited state. This difference, called the anharmonicity, is retained in flux qubits even for large capacitances, unlike in the case of transmons. The large anharmonicity, combined with low charge noise susceptibility, allows multiple levels

to be used in quantum computing, making it possible for the flux qubit device to be used either as a two-level qubit, or a three-level qutrit.

## 2.3 Flux Qubit Control and Readout

Flux qubits are controlled using time-dependent voltage signals $V(t)$ or currents $I(t)$ coupled capacitively to the circuit in the case of $V(t)$ or inductively in the case of $I(t)$. For the three-pad CSFQ presented in Section 2.2.2, and following the general Hamiltonian in equation 2.13, $C_{ij}$ and $L_{ij}$ are modified to account for coupling capacitances. Let $C'_{ij}$ denote the matrix after including the drive line capacitances. Section 2.6 gives an example of this with the $V(t)$ term. The modified capacitance matrix is

$$C'_{ij} = C_{ij} + \begin{pmatrix} C_{2d} & 0 & C_{2d} \\ 0 & C_{3d} & C_{3d} \\ C_{2d} & C_{3d} & C_{1d} + C_{2d} + C_{3d} \end{pmatrix}. \tag{2.17}$$

$V(t)$ couples to the momenta via the coupling capacitances $C_i$, [10]. This yields the Hamiltonian

$$H = \frac{1}{2\Phi_0^2}(p_i - C_i V(t))C'^{-1}_{ij}(p_j - C_i V(t)) - \Phi_0 I_{c,n} \cos\gamma_n, \tag{2.18}$$

where $C_i$ are the coupling capacitances. Unlike Section 2.2.1, $V(t)$ couples to multiple islands, so $C_i$ is determined by

$$C_i = \begin{pmatrix} 0 & 1 & 0 \\ 0 & 0 & 1 \\ 1 & 1 & 1 \end{pmatrix} \begin{pmatrix} C_{v,1} \\ C_{v,2} \\ C_{v,3} \end{pmatrix}, \tag{2.19}$$

where $C_i$ is written in the $(\gamma_{21}, \gamma_{31}, \gamma_{10})$ basis, and $C_{v,k}$ is the capacitance between $V(t)$ and the node $k$ in Figure 2.3 (a). The control Hamiltonian can be found by analyzing equation 2.18 about $V(t) = 0$, and the transition strengths between states $|m\rangle$ and $|n\rangle$, are

$$\Omega_{mn}(t) = \left\langle m \left| \frac{\partial H}{\partial V} \right| n \right\rangle V(t). \tag{2.20}$$

By switching on $V(t)$ with the appropriate frequency, one can resonantly drive transitions between eigenstates of the Hamiltonian, and so control the qubit. For two-level subspaces

of the device, define the Pauli operators as

$$\sigma_x^{mn} = |m\rangle\langle n| + |n\rangle\langle m| \tag{2.21}$$
$$\sigma_y^{mn} = i(|m\rangle\langle n| - |n\rangle\langle m|) \tag{2.22}$$
$$\sigma_z^{mn} = |m\rangle\langle m| - |n\rangle\langle n|\,. \tag{2.23}$$

For two-level transitions, the Hamiltonian simplifies to

$$H = -\frac{1}{2}\omega_{mn}\sigma_z^{mn} + \frac{1}{2}\left(\mathrm{tr}\left(\frac{\partial H}{\partial V}\sigma_x^{mn}\right)\sigma_x + \mathrm{tr}\left(\frac{\partial H}{\partial V}\sigma_y^{mn}\right)\sigma_y\right)V(t), \tag{2.24}$$

where $\omega_{mn} = \langle m|H|m\rangle - \langle n|H|n\rangle$. The drive strength is linearly proportional to the applied voltage. When multilevel transitions involving more than two states are concerned, two-photon oscillations [19] and level shifts [11] also become important at large drive strengths.

To read the CSFQ state, one can capacitively couple a resonator to the circuit, and perform dispersive readout [20]. Again, $C_{ij}$ must be modified to take the resonator capacitance into account, just as was done with the control line. The qubit-resonator coupling produces a Jaynes-Cummings type interaction

$$H_{\mathrm{int}} = g\sigma_x^{mn}(a + a^\dagger), \tag{2.25}$$

where $a$ ($a^\dagger$) is the annihilation (creation) operator of the resonator. The coupling strength $g$ can be determined by treating the resonator as a capacitive coupling to a zero-point voltage $V_0 = \sqrt{\frac{\hbar\omega}{C}}$, where $\omega$ is the resonance frequency, and $C$ is the capacitance of the resonator. In the limit where the resonator and the transition are far detuned from each other, known as the dispersive regime, the resonator will experience a frequency shift $\chi = 2g^2/\Delta$, depending on whether the qubit is in state $|1\rangle$ or $|0\rangle$. Measuring the resonator frequency performs a non-demolition projective measurement [5, Sec. 2.2.5] of the qubit state [21].

In experiments, the readout resonator frequency is measured by driving the readout resonator at its resonance frequency. The signal coming out of the readout resonator is then down-converted to in-phase and quadrature components using an IQ mixer, such that the resonator frequency is mixed down to a DC signal. The qubit state is then determined by measuring the average voltage $\langle V\rangle$ of the readout signal. If the qubit is in state $|0\rangle$, the voltage is higher than if the qubit is in state $|1\rangle$, since the frequency shift of the resonator gives an AC signal after being mixed down, lowering the average readout voltage. $V$ is the observable for the qubit state. Around $10^4$ measurements of $V$ are done for each data point in order to average the noisy readout signal.

## 2.4 Sources of Decoherence

Decoherence is the loss of information in a quantum system caused by unknown irreversible interactions between the system and its environment [5, Sec. 8.2.2]. These interactions are modelled as memoryless (Markovian) dissipative processes, or as fluctuating parameters in the circuit Hamiltonian. For a system with density operator $\rho$, the master equation

$$\dot{\rho} = \frac{i}{\hbar}[\rho, H] + L_i \rho L_i^\dagger - \frac{1}{2}\left(L_i^\dagger L_i \rho + \rho L_i^\dagger L_i\right) \tag{2.26}$$

accounts for dissipation through the collapse operators $L_i$. In general, any stray signal coupled to the system causes decoherence [5, Sec. 8.4.1]. Therefore, noise sources can be modelled by adding noisy $V(t)$ and $I(t)$ signals at appropriate points in the circuit model of a qubit. The two dominant sources of noise in the three-pad CSFQ are charge noise and flux noise.

Dissipative processes can be classified into dephasing and relaxation processes. For a two-level subspace spanned by the eigenvectors $|m\rangle$ and $|n\rangle$ of the circuit Hamiltonian $H$, with $\langle m|H|m\rangle > \langle n|H|n\rangle$, the dephasing collapse operator is $L = \sqrt{\Gamma_{\phi_{mn}}}\sigma_z^{mn}$, where the relaxation rate $\Gamma$ is

$$\Gamma_{\phi_{mn}} = \frac{1}{2\hbar^2}|\langle m|A|m\rangle - \langle n|A|n\rangle|^2 S(0). \tag{2.27}$$

$A$ is the interaction operator between the circuit and the noise source, and $S(0)$ is the noise power spectral density (PSD) of the at zero frequency [22, Sec. 3]. White noise sources have PSDs independent of frequency, and $1/f$ noise sources have PSDs proportional to $\frac{1}{\omega^\alpha}$.

The relaxation process $|m\rangle$ to $|n\rangle$ has a collapse operator

$$L = \sqrt{\Gamma_{|m\rangle\to|n\rangle}}\,|m\rangle\langle n| \tag{2.28}$$

with associated rate

$$\Gamma_{|m\rangle\to|n\rangle} = \frac{1}{\hbar^2}|\langle m|A|n\rangle|^2 S(\omega_{mn}). \tag{2.29}$$

Following detailed balance, each relaxation processes has an associated reverse process

$$L = \sqrt{\Gamma_{|n\rangle\to|m\rangle}}\,|n\rangle\langle m| \tag{2.30}$$

with rate

$$\Gamma_{|n\rangle\to|m\rangle} = \exp\left(-\frac{\hbar\omega_{mn}}{k_B T}\right)\Gamma_{|m\rangle\to|n\rangle}, \tag{2.31}$$

where $k_B$ is Boltzmann's constant and $T$ is the temperature of the device [23, Sec. 3.b]. From equation 2.26, relaxation drives the qubit to the equilibrium state

$$\rho_{\text{eq}} = \frac{\exp\left(-\frac{H}{k_B T}\right)}{\text{tr}\,\exp\left(-\frac{H}{k_B T}\right)}, \tag{2.32}$$

which, though detrimental for coherence, is useful for state preparation.

For the case of two-level systems, relaxation rates are quoted using the $T_1$ and $T_2^*$ decay parameters [24, Sec. A.3]. $T_1$ gives the rate at which a system prepared in $|1\rangle\langle 1|$ decays to $\rho_{\text{eq}}$, and $T_2^*$ gives the rate at which components of $\rho$ in the $\frac{1}{\sqrt{2}}(|0\rangle + |1\rangle)$ state decay. $T_1$ and $T_2^*$ are given by

$$T_1 = \left(\Gamma_{|0\rangle\to|1\rangle} + \Gamma_{|1\rangle\to|0\rangle}\right)^{-1} \tag{2.33}$$

and

$$T_2^* = \left(\frac{1}{2T_1} + \Gamma_{\phi_{01}}\right)^{-1}. \tag{2.34}$$

The challenge of quantum control is to perform as many operations as accurately as possible within a reasonable fraction of $T_1$, beyond which the qubit loses coherence.

In flux qubits, two dominant noise mechanisms are charge noise and flux noise. Charge noise is caused by stray voltages accumulating on capacitive elements in superconducting devices [9, Sec. 2]. Examples of these include two-level systems in the Josephson junction dielectric barrier and local fluctuations caused by microscopic effects on capacitive pads. This noise shows up as a fluctuating parameter $n_g$ in the Hamiltonian, which can be modelled as a capacitive coupling to the CSFQ. Effects of charge noise can be reduced by decreasing $E_C$. Flux noise is noise caused by stray magnetic fields from environment dipoles or current noise in flux biasing. This can be suppressed by increasing the aspect ratio of the superconducting loop in the persistent current qubit [25].

## 2.5 Measuring CSFQ Properties

This section discusses how to determine the flux qubit Hamiltonian, control, readout, and noise parameters experimentally. The first step is to obtain the transmission spectrum of the readout resonator versus the magnetic flux bias. This determines the readout resonator frequency, the location of the symmetry point, and the coupling strength $g$. Figure 2.4 (a) shows the transmission spectrum through the readout resonator versus the applied voltage to an external magnetic flux biasing coil.

The next step is to perform transmission spectroscopy, applying a low-power control signal $V(t) = V\cos(\omega t)$. Resonance occurs when $\omega = \omega_{01}$. Figure 2.4 (b) shows spectroscopy around the $\omega_{01}$ transition. This yields $\omega_{01} = 2\pi \times 1.1465\,\text{GHz}$. Control signals at frequency $\omega_{01}$ are optimal for applying quantum gates, as the largest population transfer occurs when $V(t)$ is resonant.

After determining $\omega_{01}$, a Rabi experiment [10] is used to measure the Rabi frequency $\Omega_{01}$. Applying $V(t)$ at $\omega_{01}$ causes the qubit state $|\psi\rangle$ to oscillate between $|0\rangle$ and $|1\rangle$ with frequency $\Omega_{01}$. Therefore, applying $V(t)$ with frequency $\omega_{01}$ for duration $\Omega_{01}/2$ realizes an $X_{01} = |0\rangle\langle 1| + |1\rangle\langle 0|$ quantum gate [5, Sec. 4.2]. Applying $V(t)$ for duration $\Omega_{01}/4$ realizes an $H_{01} = |+\rangle\langle 0| + |-\rangle\langle 1|$ gate, where

$$|\pm\rangle = \frac{1}{\sqrt{2}}\left(|0\rangle \pm |1\rangle\right). \tag{2.35}$$

Figure 2.4 (c) shows the $|0\rangle \to |1\rangle$ Rabi experiment, with the $X_{01}$ gate time labelled.

Spectroscopy with a $X_{01}$ gate applied prior to the spectroscopy pulse then follows in order to find $\omega_{12}$. A Rabi experiment on $\omega_{12}$ then finds $X_{12}$. In this way, spectroscopy and control can be determined up to any desired level, limited by coherence and available control frequencies. Higher-amplitude drives also identify two-photon transitions. Figure 2.4 shows spectroscopy and Rabi experiments for the 12 and the 02 two-photon transition in addition to the 01 transitions.

In addition to gate times, $\rho_{\text{eq}}$ is determined by comparing Rabi oscillation amplitudes. Assume the circuit starts in $\rho_{\text{eq}}$ as in equation 2.32, and $\langle 2|\rho_{\text{eq}}|2\rangle$ is negligible. Then, the amplitude $A_1$ of the Rabi 01 experiment with an $X_{12}$ preparation pulse and the amplitude $A_2$ of the Rabi 01 experiment with an $X_{12}X_{01}$ preparation pulse ($X_{01}$ is applied first), is related to the equilibrium population by

$$\langle 0|\rho_{eq}|0\rangle = \frac{A_1}{A_1 + A_2}. \tag{2.36}$$

This measures $\rho_{\text{eq}}$. Once $\rho_{\text{eq}}$ is known, $V$ can be measured by $V$ with $\rho_{\text{eq}}$, and comparing $\text{tr}\left(V\rho_{\text{eq}}\right)$, $\text{tr}\left(\sigma_x^{01}\rho_{\text{eq}}\sigma_x^{01}V\right)$, and $\text{tr}\left(V\sigma_x^{12}\sigma_x^{01}\rho_{\text{eq}}\sigma_x^{01}\sigma_x^{12}V\right)$.

With preparation, control, and measurement parameters determined, the next step is to determine coherence parameters. Figure 2.5 (a) shows a $T_1$ experiment result. This is obtained by applying $X_{01}$ and waiting for the device to relax back to $\rho_{\text{eq}}$. Following equation 2.26 with the collapse operators in equations 2.28 and 2.30, $\langle V\rangle$ decays exponentially with rate $\frac{1}{T_1}$. A typical $T_1$ is $45\,\mu\text{s}$.

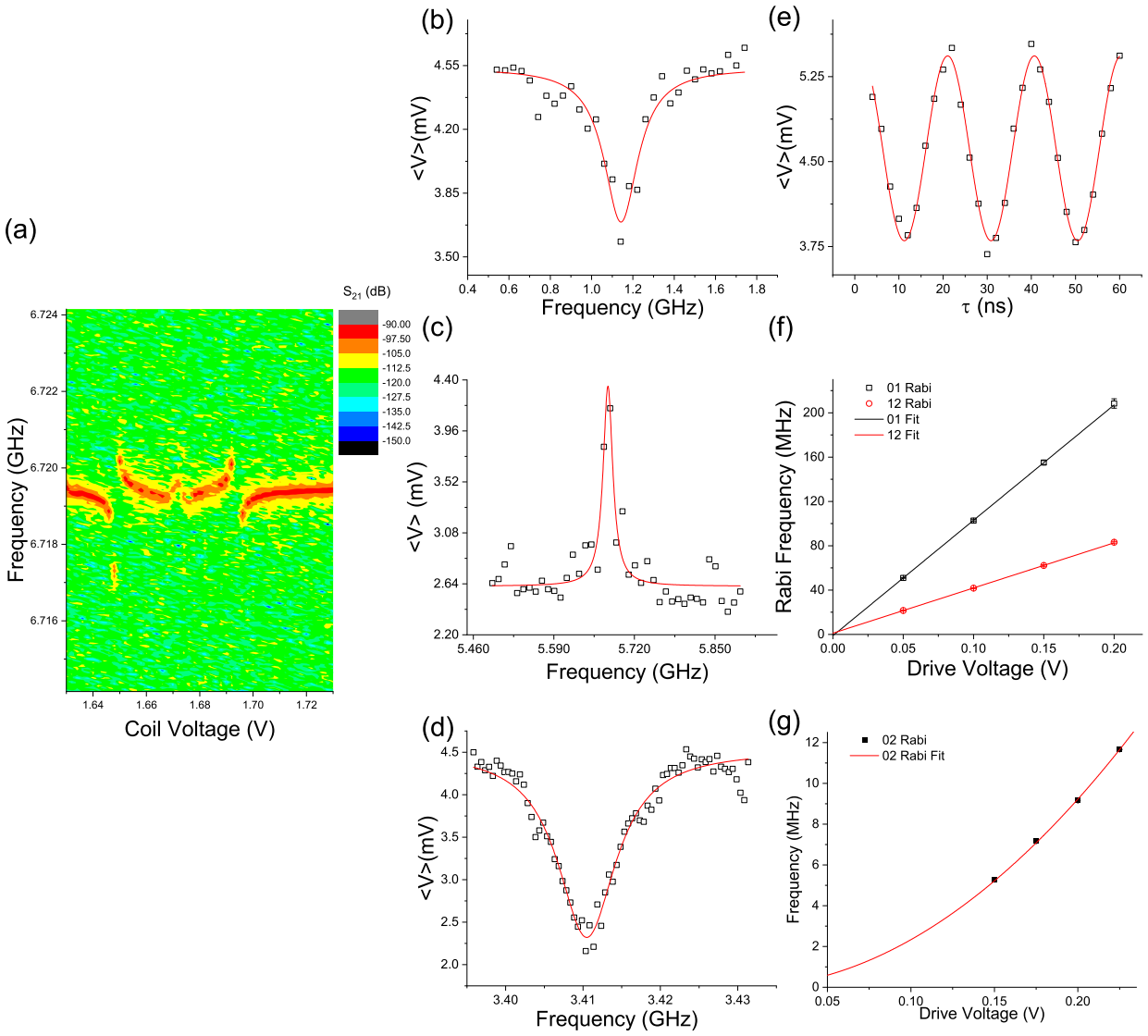


Figure 2.4: (a) The transmission spectrum of the CSFQ device versus magnetic field biasing voltage. (b-d) Low power Transmission spectroscopy, showing $\langle V_h \rangle$ versus control frequency from (top to bottom), the 01 (b), 12 (c), and 02 (d) transitions. (e) The result of a typical Rabi experiment on 01, showing $\langle V \rangle$ versus the delay time $\tau$ (f) Rabi frequency versus voltage for the 01, 12, and 02-two photon transitions. (g) Rabi frequency versus drive voltage for the 02 two-photon transition. Note the quadratic dependence of Rabi frequency on drive voltage.

Figure 2.5(b) shows a Ramsey experiment result used to obtain $T_2^*$. The Ramsey experiment is done by applying $H_{01}$, waiting some time $\tau$, applying $H_{01}$ again, and then measuring $\langle V_h \rangle$. $\langle V_h \rangle$ decays exponentially versus $\tau$, with decay constant $T_2^*$. To make the decay easier to see, the $H$ gates were applied slightly off resonance, so that the exponential decay also has a sinusoidal component. A typical $T_2^*$ was $4.5\,\mu$s.

Following the Wiener-Khinchin theorem, the autocorrelation function $\kappa(t) = \langle V(0)V(t) \rangle$ for a noise source, and its power spectral density $S(\omega)$ are Fourier transforms of each other. For white noise, $\kappa(t)$ is a Dirac delta, meaning that $V(t)$ measured at a later time is independent to the $V(t)$ measured at an earlier time. This is not the case for $\frac{1}{f}$ noise, where $V(t)$ is correlated in time. As a result, driven evolution can "undo" some dephasing, especially on short time scales. This means that $T_2^*$ is a worst case coherence time. In the best case, the qubit will not be exposed to $\frac{1}{f}$ noise during driven evolution, and so $T_2 = 2T_1$ becomes more representative of the coherence time. This effect can be seen in the spin echo experiment. It consists of the following sequence

1. $H_{01}$
2. Delay of $\frac{\tau}{2}$
3. $X_{01}$
4. Delay of $\frac{\tau}{2}$
5. $H_{01}$
6. Measurement of $\langle V \rangle$

$\langle V \rangle$ decays exponentially. The decay rate $T_{2,\text{echo}}$ is $9.0\,\mu$s.

Finally, Figure 2.5 (c) shows a multilevel relaxation plot, used to obtain the relaxation rates for all transitions in the $|0\rangle$, $|1\rangle$, and $|2\rangle$ space. This is a modification of the $T_1$ experiment, where for each delay, one measurement is taken as is, and one measurement is taken with an $\sigma_x^{12}$ pulse applied. By comparing $\langle V_h \rangle$ for both measurements, and assuming populations stay in the $\{|0\rangle, |1\rangle, |2\rangle\}$ space, the diagonal elements of $\rho$ can be determined versus the time delay. Relaxation rates were then fit to this data, yielding a three-level relaxation model for the device. Ramsey experiments on 01, 12, and the 02 transition filled in the components for pure dephasing.

Following this experiment setup, the transition frequencies, Rabi frequencies, equilibrium state, voltage observable, and a coherence model are now known. One now has all the tools needed to perform and characterize gate sets on the CSFQ device.

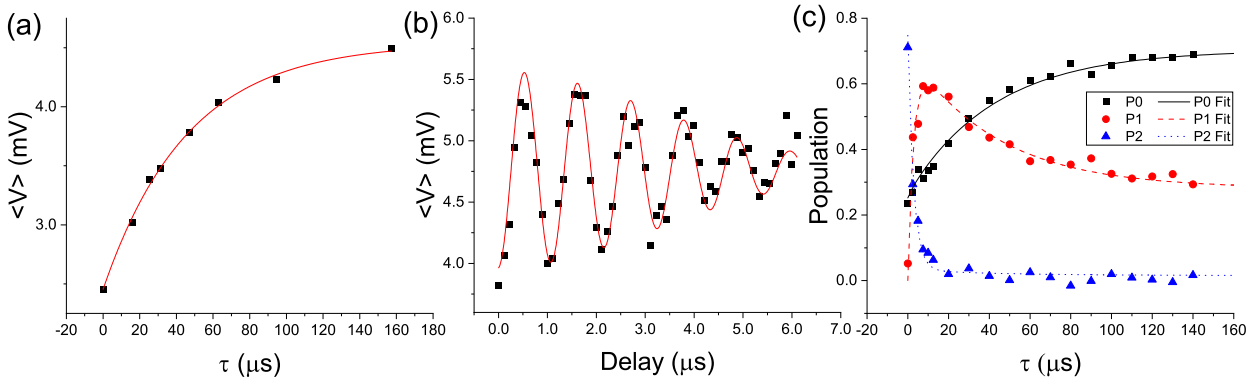


Figure 2.5: (a) A typical $T1$ experiment result, with $T_1 = 46.1 \pm 2.5\,\mu$s. (b) A typical Ramsey experiment result, with $T_2^* = 4.7 \pm 0.3\,\mu$s. (c) The multi-level relaxation result

## 2.6 Characterizing Gates on a CSFQ

### 2.6.1 The Average Gate Fidelity

A quantum gate, or channel, maps density operators to density operators [5, Sec. 8.2]. A gate mapping a $d$-dimensional density matrix to another $d$-dimensional density matrix requires $d^4$ real coefficients to specify [26]. The most complete description of a quantum gate therefore consists of a list of these coefficients, but the data needs to be summarized to get a figure of merit for the gate performance. What is needed is a function that takes in two gates and returns a number indicating how well one gate implements another, with an operationally-useful definition.

For seeing how well a state $\rho$ matches a state $\sigma$, such a quantity is readily available in terms of the fidelity $F(\rho, \sigma)$, given by [5, Sec. 9.2.2]

$$F(\rho, \sigma) = \mathrm{tr}\sqrt{\sqrt{\rho}\sigma\sqrt{\rho}}. \tag{2.37}$$

$F(\rho, \sigma)$ gives the probability of $\rho$ passing a test to identify as $\sigma$. To get an equivalent measure for two gates $\Lambda_1$ and $\Lambda_2$, one can consider $F(\Lambda_1(\rho), \Lambda_2(\rho))$, but this leaves an open question of which $\rho$ to use [27]. For finite-dimensional $\rho$, this problem is solved by averaging $F(\Lambda_1(\rho), \Lambda_2(\rho))$ over all pure states (i.e. states where $\rho = |\psi\rangle\langle\psi|$ for some $|\psi\rangle$), yielding the average gate fidelity $\mathcal{F}(\Lambda_1, \Lambda_2)$ [28].

Just as density operators $\rho$ inhabit a space of possible operators, so too do quantum gates. In the case of unitary gates, i.e. those $\Lambda$ for which a $\Lambda^\dagger$ exists such that $(\Lambda \circ \Lambda^\dagger)(\rho) =$

$\rho$, the space of unitary operators has an $SU(d)$ group structure. If $d$ is finite, this also implies there exists a unique uniform measure $\mu$ on this space, relative to which one can integrate [29]. This means uniform random sampling over pure states in $SU(d)$ is possible, and allows definition of the Haar average $W$ of $\Lambda$ as

$$W(\Lambda)(\rho) = \int (\mathcal{U} \circ \Lambda \circ \mathcal{U}^\dagger)(\rho)\, \mathrm{d}\mu(\mathcal{U}). \tag{2.38}$$

The Haar average rigorously assigns a "surface area" to a set of operators in $SU(d)$. For qubits, the analogy of the Haar average is that it measures the surface area of the Bloch sphere [5, Sec. 1.2]. $W(\Lambda)$ is invariant under unitary transformations [28], since $\mu(\mathcal{U})$ is uniform. For qubit unitary channels, the analogy of equation 2.38 is that the Bloch sphere has the same surface area regardless of whether measurement starts at the north or south pole. Haar averaging over unitary operators is equivalent to Haar averaging over pure states, since

$$\int \langle\phi|\Lambda(|\phi\rangle\langle\phi|)|\phi\rangle \ \mathrm{d}\mu(|\phi\rangle\langle\phi|) = \int \langle 0|U^\dagger \Lambda(U\,|0\rangle\langle 0|\,U^\dagger)U|0\rangle \ \mathrm{d}\mu(U). \tag{2.39}$$

The average gate fidelity is therefore

$$\mathcal{F}(\Lambda_1, \Lambda_2) = \int F\left((\Lambda_1 \circ \mathcal{U})\left(|0\rangle\langle 0|\right), (\Lambda_2 \circ \mathcal{U})\left(|0\rangle\langle 0|\right)\right) \mathrm{d}\mu(\mathcal{U}) \tag{2.40}$$

and if $\Lambda_2$ is unitary, then $\mathcal{F}(\Lambda, \mathcal{U}) = \mathcal{F}(\mathcal{U}^\dagger \circ \Lambda, \mathcal{I})$, where $\mathcal{I}$ is the identity map, and

$$\mathcal{F}(\Lambda, \mathcal{U}) = \langle 0|W(\mathcal{U}^\dagger \circ \Lambda)(|0\rangle\langle 0|)|0\rangle\,. \tag{2.41}$$

Following [28], $\mathcal{F}(\Lambda, \mathcal{U})$ simplifies to

$$\mathcal{F}(\Lambda, \mathcal{U}) = \frac{1}{d^2(d+1)} \sum_{P \in \mathcal{P}_d} \mathrm{tr}\left(P^\dagger U^\dagger \Lambda(P) U\right) + \frac{1}{d+1} \tag{2.42}$$

where $U$ is the unitary operator associated with $\mathcal{U}$, and $\mathcal{P}_d = \langle X_d, Z_d \rangle$ is the Pauli group. Given two copies of a random pure state, one of which is sent through $\Lambda$, and the other through $\mathcal{U}$, $\mathcal{F}(\Lambda, \mathcal{U})$ gives the expected fidelity between the two states that come out of $\Lambda$ and $\mathcal{U}$. A higher $\mathcal{F}(\Lambda, \mathcal{U})$ therefore indicates that $\Lambda$ is a better implementation of $\mathcal{U}$ in a meaningful way.

### 2.6.2 Quantum Process Tomography

Quantum process tomography (QPT) is a means of obtaining all $d^4$ coefficients of $\Lambda$ by measuring the output state $\rho_{\text{out}} = \Lambda(\rho_{in})$ for $d^2$ different linearly-independent (i.e. the different $\rho$ cannot be related by scalar multiplication) $\rho_{\text{in}}$ input states [30]. Given a measurement $V$, a set of $X$ and $H$ gates, and many copies of $\rho$, one can measure all the coefficients of $\rho$ by performing $d^2$ experiments. This requires assuming that $X$ and $H$ are implemented to high average gate fidelity, so that for an experimental implementation $\Lambda_{\text{prep}}$ of a preparation gate $U_{\text{prep}}$,

$$\text{tr}(U_{\text{prep}}\rho U_{\text{prep}}^{\dagger}V) = \text{tr}(\Lambda_{\text{prep}}(\rho)V). \tag{2.43}$$

Expressing $\rho$ in an orthogonal basis of operators like the Pauli group allows the effect of all $d^2$ operators $U$ to be calculated, and thus determine the unique $\rho$ that produces the set of measurements $\text{tr}(\Lambda_{\text{prep}}(\rho)V)$. This is quantum state tomography (QST). Performing this with $d^2$ different $\rho$, and taking QST on each of theses $\rho$ then gives the $d^4$ coefficients of the gate $\Lambda$. This is quantum process tomography (QPT). QPT is the gold standard for characterizing gates, and has the advantage of yielding the entire process matrix, but it only characterizes one gate, and it is a slow procedure, especially when compared with randomized benchmarking (RB). Furthermore, the assumption of equation 2.43 means QPT cannot distinguish between errors intrinsic to the gate and state preparation and measurement (SPAM) errors.

### 2.6.3 Randomized Benchmarking

Randomized benchmarking (RB) is an alternate means of characterizing gate sets compared to QPT. It is a set of experiment protocols consisting of taking a state, applying a set of randomly-chosen gates to it, inverting the set of randomly-chosen gates to ideally prepare some final state, and then measuring [6, p. 3]. RB protocols yield less information about individual gates than QPT, but they can return results faster, and in a manner robust to state preparation and measurement errors. Two tools in RB that enable this are Haar averaging, and unitary $t$-designs.

Following [29], the Haar average $W(\Lambda)$ of a map $\Lambda$ as presented in Section 2.6.1 is a depolarizing channel. This means that for all $\rho$, there is some $p$ such that

$$W(\Lambda)(\rho) = p\rho + (1-p)\text{tr}\left(I_d\rho\right)\frac{I_d}{d} + K(\rho), \tag{2.44}$$

where $I_d$ is the identity operator on the $d$-dimensional space that was Haar-averaged. $K(\rho)$ is a leftover term, which must be invariant under unitary transformations on the Haar-averaged space, and satisfy

$$\mathrm{tr}\left(K(\rho)\right) = (1-p)(1-\mathrm{tr}\left(I_d\rho\right)). \tag{2.45}$$

If $p$ is large, then $K$ is negligible, making $W(\Lambda)(\rho)$ a depolarizing channel robust to small leakage out of the Haar-averaged space. If $\Lambda$ is a noisy implementation of the identity map $\mathcal{I}$, then

$$\mathcal{F}(\Lambda, \mathcal{I}) = p + \frac{1-p}{d}. \tag{2.46}$$

Taking $n$-fold compositions of $\Lambda$ is then equivalent to composing depolarizing channels, yielding

$$W(\Lambda)^{\circ n}(\rho) = p^n\rho + (1-p^n)\frac{I}{d} \tag{2.47}$$

and which then allows $p$ to be determined from the exponential decay of $\langle V\rangle$ as a function of $n$, as the state depolarizes. Since depolarizing channels are invariant under unitary transformations, this depolarization will be visible regardless of errors in preparing or measuring $\rho$.

Depolarization is now robust to SPAM error because of unitary invariance of $W(\Lambda)$, but the question how to sample from $W(\Lambda)$ still remains. Fortunately, the Clifford group $\mathcal{C}_d$, consisting of all operators that map Pauli operators $\mathcal{P}_d$ to Pauli operators, has the 2-design property. This means

$$W(\Lambda)(\rho) = \frac{1}{|\mathcal{C}_d|}\sum_{C\in\mathcal{C}_d} C^\dagger\Lambda(\rho)C \tag{2.48}$$

Since $\mathcal{C}_d$ is finite, one can therefore sample from this group, and construct depolarizing channels. $\Lambda$ is then a map from the ideal Clifford group to the real Clifford group as implemented on the device, and so $\mathcal{F}(\Lambda, \mathcal{I})$ measures how well the Clifford gates are implemented on average.

The RB experiment therefore consists of taking the initial state $\rho_{\mathrm{eq}}$ and applying $n-1$ random Clifford gates. Next, an inversion gate is applied to make the sequence map to the identity operator, and then $V$ is measured. Note that an inversion operator also exists, owing to the Clifford group property. Repeating this many times for each $n$ gives the average $\langle V\rangle$ measured as

$$\mathrm{tr}(W(\Lambda)^{\circ n}(\rho_{\mathrm{eq}})V) = p^n\mathrm{tr}(\rho_{eq}V) + (1-p^n)\mathrm{tr}\left(\frac{I}{d}V\right) \tag{2.49}$$

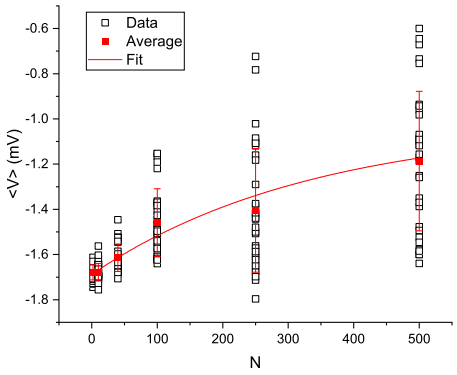


Figure 2.6: A result for qubit RB on the 01 space of the CSFQ.

which can be re-written as

$$\langle V \rangle (n) = \mathrm{tr}\left(\left(\rho_{\mathrm{eq}} - \frac{I}{d}\right) V_h\right) p^n + \mathrm{tr}\left(\frac{I}{d} V\right). \tag{2.50}$$

The average fidelity can then be found using equation 2.46. This fidelity determines how far away the error $\Lambda$ in implementing a Clifford group is from the identity map, and so the higher the value, the better the control scheme is in implementing Clifford gates on average. This is a desirable property of a control scheme, and it can be measured over the set in a single exponential decay, as opposed to the hundreds of QPT experiments required to get the same quantity [27].

Figure 2.6 gives an RB result on the qubit, plotting $\langle V \rangle$ versus the number of Clifford gates. $\langle V \rangle$ was read on the Q quadrature. The initial value $\langle V \rangle$ corresponds to $\mathrm{tr}(V \rho_{\mathrm{eq}})$, the final value corresponds to $\mathrm{tr}\left(V \frac{I}{2}\right)$, and the exponential decay gives a fidelity of $99.92 \pm 0.03\,\%$. This shows that the control is strong enough that it can implement a depolarizing channel using Clifford gates to high fidelity. Note that some gates in the Clifford gate set may be implemented to higher fidelity than others. Evidence for good gate implementations comes from other experiments, like interleaved RB [31], or QPT.

# Chapter 3

# Qutrit Randomized Benchmarking

This chapter describes an experiment characterizing qutrit control using randomized benchmarking (RB). RB is a protocol that yields the average error for the elements of the Clifford group. We implement qutrit gates using a universal decomposition method that can be used to generate any unitary for a qutrit and more generally for qudits of any dimension. The measured average fidelity is $\bar{\mathcal{F}} = 99.0 \pm 0.2\%$ for members of the qutrit Clifford group $\mathcal{C}_3$. In addition, we characterize a subset of the Clifford group using quantum process tomography (QPT), which provides an independent verification of the unitary synthesis method and yields results in agreement with RB. Analysis of this experiment revealed errors due to level shifts, leakage, and decoherence. Level shifts, which do not lead to significant errors in the usual case of resonant control in a two-dimensional subspace, are the dominant source of errors, pointing to relevant future work on shaped control pulses for qudits.

## 3.1 The Randomized Benchmarking Experiment

Recent advances in large-scale quantum information processors have relied on manipulating quantum information using two-level systems as qubits [32, 33, 34, 35]. Theoretical work shows that using multilevel systems as qudits offers performance advantages in quantum error correction [36, 37, 38, 39], quantum sensing [40, 41], and quantum communication [42]. Efficient universal qudit control required for these applications follows from an extension of the Solovay-Kitaev theorem from the qubit unitary group SU(2) to the qudit group SU($d$), where $d$ is the dimension of the qudit's Hilbert space [43]. However, implementation of such control brings new challenges including mapping qudit gates to experimentally-accessible

controls, and understanding how control errors influence the type and amount of errors in a qudit gate. Characterizing qudit gates is also more resource-intensive than characterizing qubit gates because the larger Hilbert space allows more complex states to form.

The qutrit randomized benchmarking experiment is performed on a variant of a capacitively-shunted flux qubit that combines relatively long coherence times with high anharmonicity [10]. Anharmonicity is the difference between the second and first transition frequencies. A qutrit is encoded in the lowest three energy states of the device, denoted by $|0\rangle$, $|1\rangle$, and $|2\rangle$. The large anharmonicity enables fast selective driving of the $|0\rangle - |1\rangle$ and $|1\rangle - |2\rangle$ transitions. Qutrit control is done using microwave pulses sent via a coplanar waveguide coupled capacitively to the device (see Fig. 3.1 (a)). Application of a microwave pulse resonant with the $|m\rangle - |n\rangle$ transition implements a rotation $R(\theta)^{nm}_{\phi}$ in the two dimensional space formed by states $|m\rangle$ and $|n\rangle$, where $\theta$ is the rotation angle and $\phi$ is the rotation axis phase. Control pulses are generated using direct synthesis by a large bandwidth arbitrary waveform generator, model Tektronix AWG 70001. Using large bandwidth direct synthesis enables the use of sequences of short pulses with widely different carrier frequencies. The device state is measured using homodyne readout of a coplanar waveguide resonator also coupled capacitively to the device. The readout voltage, averaged over many repetitions, corresponds to the expectation value of the operator $V = V_0 \, |0\rangle\langle 0| + V_1 \, |1\rangle\langle 1| + V_2 \, |2\rangle\langle 2|$. State preparation is done by waiting for the device to relax to the thermal state $\rho_{\text{th}} = P_{\text{th},0} \, |0\rangle\langle 0| + P_{\text{th},1} \, |1\rangle\langle 1|$, where $P_{\text{th},n} = \langle n|\rho_{\text{th}}|n\rangle$. We assume that higher state populations are negligible, in line with the large transition frequency between states $|1\rangle$ and $|2\rangle$. The thermal excited state population $P_{\text{th},1}$ and the readout voltage levels $V_0$, $V_1$, and $V_2$ are measured using a protocol based on observing $|0\rangle - |1\rangle$ Rabi oscillations starting with initial states based on the thermal state with additional population swaps (see Section 3.2 and Ref. [10]).

Performing a qudit gate $U$ requires a decomposition of $U$ that can be mapped to the available controls, which becomes more difficult as $d$ increases. In this chapter we use an approach that decomposes $U$ into products of Givens rotations $R(\theta)^{mn}_{\phi}$, where Givens rotations are unitaries in two-dimensional subspaces of the qudit space. This approach is universal for qudits of any dimension $d$ and only requires the availability of Givens rotations for $d-1$ pairs of states that span the full Hilbert space [44]. The decomposition $U$ has two main steps. In the first step, Givens rotations are identified that, when multiplying the unitary $U$ in succession, lead to step-by-step cancellation of the off-diagonal elements of $U$, yielding a diagonal matrix. A maximum number of $\frac{1}{2}d(d-1)$ Givens rotations, one corresponding to cancellation of each element in the upper diagonal block, is required. In the second step, $d-1$ phase gates multiply the resulting diagonal matrix, yielding the identity matrix up to a phase factor. Each phase gate requires three Givens rotations, for a total of $3(d-1)$ rotations (see Section 3.2). Decomposing a qutrit gate requires up to

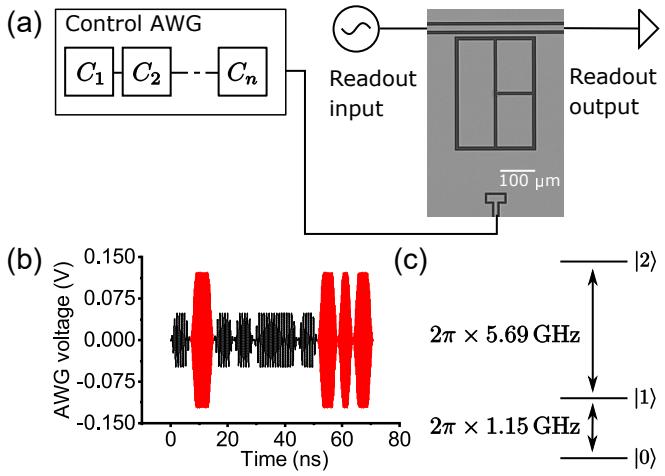


Figure 3.1: A representation of the experiment setup. (a) A scanning electron micrograph of the device on which the experiment was performed, with connections to the control AWG and the readout setup shown. The control AWG is synthesizing a sequence of Clifford gates $C_1$ to $C_n$ for an RB experiment. (b) The waveform for a Walsh-Hadamard gate $H_3$ as outputted by the control AWG. Black (dark) lines indicate $|0\rangle - |1\rangle$ driven transitions and red (light) lines indicate $|1\rangle - |2\rangle$ driven transitions (c) A level diagram for the qutrit, with transition frequencies shown.

9 Givens rotations. Each Givens rotation $R(\theta)_{\phi}^{mn}$ is then mapped to a pulse generated by the AWG with the pulse envelope area proportional to $\theta$, the frequency resonant with the $mn$ transition, and the phase given by $\phi$. The control Hamiltonian for $R(\theta)_{\phi}^{mn}$ is $H_{\text{drive}} = \frac{1}{2}\Omega_{mn}e^{-i\phi}\left|m\right\rangle\!\left\langle n\right| + \text{h.c.}$, where $\Omega_{mn}$ is the drive strength for the $m-n$ transition. Each pulse has a cosine-shaped rise and fall envelope with $t_{\text{rise}} = t_{\text{fall}} = 2\,\text{ns}$. Figure 3.1 (b) shows the waveform for a qutrit Walsh-Hadamard gate $H_3$ at $\Omega_{01} = \Omega_{12} = 2\pi \times 50\,\text{MHz}$ synthesized using this decomposition [11].

The approach for implementing an arbitrary unitary is verified using QPT for a set of representative gates, following the procedure from Ref. [11]. QPT is a standard technique for finding the process matrix of a black box [30], and so the gate fidelity [28] determined from the process matrix determines whether a qutrit gate performs as intended. The Walsh-Hadamard gate $H_3$, the generalized phase gate $S_3$, and the generalized Pauli gates $X_3$ and $Z_3$ are characterized. $H_3$ and $S_3$ are chosen because they generate the qutrit Clifford group. $X_3$ and $Z_3$ are chosen because they generate the Pauli group $\mathcal{P}_3$ [45]. The gate fidelities for $H_3$, $S_3$, $X_3$ and $Z_3$ are 96.0%, 98.4%, 99.0%, and 99.0%, respectively, showing that the experimental implementation of the gate decomposition synthesizes the intended gates. We attribute the discrepancy between the individual gate fidelities from QPT and the average gate fidelity from RB to state preparation and measurement (SPAM) error, and due to $H_3$ requiring more Givens rotations to synthesize than $X_3$ or $Z_3$. Figure 3.5 in Section 3.3 shows the gate decompositions found for these gates.

Next, the average fidelity $\bar{\mathcal{F}}$ of $\mathcal{C}_3$ is characterized using RB. RB relies on the fact that a sequence of $l$ random gates selected from $\mathcal{C}_3$, such that their product is the identity operator, behaves on average as a depolarizing channel with the same $\bar{\mathcal{F}}$ as $\mathcal{C}_3$ [29, 27]. Therefore, measuring $\langle V\rangle$ versus $l$ determines $\bar{\mathcal{F}}$ via the model

$$\langle V\rangle = (V_i - V_f)\left(\frac{d\bar{\mathcal{F}} - 1}{d-1}\right)^{l} + V_f, \tag{3.1}$$

where $V_i$ ($V_f$) is $\langle V\rangle$ at $l = 0$ ($l = \infty$), and $d = 3$ is the dimension of the qudit [46]. RB is used because it measures $\bar{\mathcal{F}}$ faster than QPT, at the expense of not giving information about individual gates in $\mathcal{C}_3$ [27]. Based on the fact that $H_d$ and $S_d$ generate $\mathcal{C}_d$ for any prime $d$ [47], the set $\mathcal{C}_3$ is generated by taking products of $H_3$ and $S_3$ until no new elements are obtained. The group generated in this way has 216 elements, as expected. Each Clifford gate used in RB is decomposed into Givens rotations using the decomposition presented above. Figure 3.2 (a) plots the experimentally-determined $\langle V\rangle$ versus $l$ for ten randomizations at each $l \in \{2, 6, 10, 20, 50, 100, 200\}$, with $\Omega_{01} = \Omega_{12} = 2\pi \times 50\,\text{MHz}$. The measured $\bar{\mathcal{F}} = 99.0 \pm 0.2\%$ indicates that the members of $\mathcal{C}_3$ are implemented to high

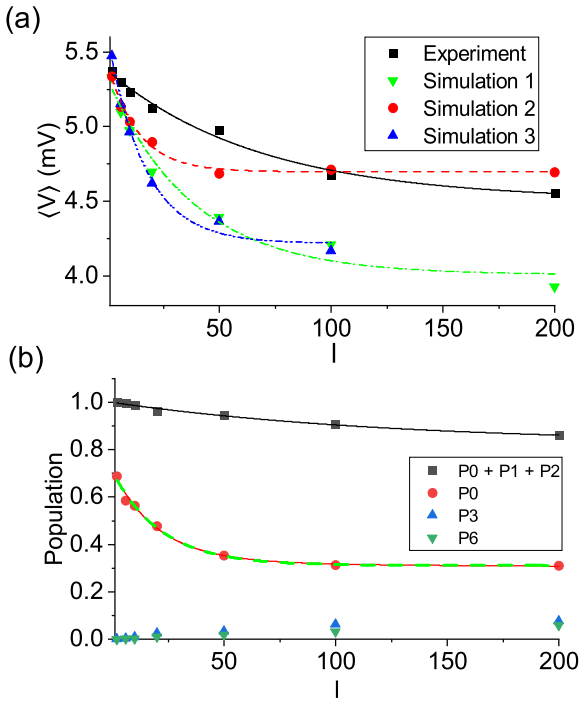


Figure 3.2: Experiment and simulated results for qutrit RB. (a) The experimentally-measured $\langle V \rangle$ compared to three simulation results. Simulation 1 is the numerically-simulated result. Simulation 2 is like Simulation 1, but with $V_3$ and $V_6$ optimized to match experiment data. Simulation 3 is like Simulation 1, but with decoherence modelled as well. Fits to equation 3.1 are shown for the experiment and each simulation. (b) The populations from Simulation 1 with the leakage analysis from [3] performed on them. The dashed line is an exponential fit for $P_0$ vs $l$.

fidelity on average. Uncertainties are quoted to one standard deviation. Increasing $\Omega_{01}$ and $\Omega_{12}$ to $2\pi \times 97.38\,\text{MHz}$ leads to a lower fidelity of $97.3 \pm 0.3\%$. Scaling the drive voltages by $\pm 3\%$ to correct for possible over-rotations in 01 and 12 neither significantly affects the fidelity, nor does it lead to a clear optimal result.

Since $\mathcal{C}_3$ is finite, each element of $\mathcal{C}_3$ has a finite, characteristic order. Repeatedly applying a gate $N$ times therefore nominally produces a $\langle V \rangle$ signal periodic in $N$, with the period equal to the order of the element. $H_3$, $S_3$, $X_3$, and $Z_3$ are repeatedly applied to observe this periodic behaviour. For $S_3$ and $Z_3$, an $H_3$ gate is prepended and appended to the sequence to produce a $\langle V \rangle$ signal varying with $N$. Figure 3.3 shows the experimentally-measured $\langle V \rangle$ versus the value expected from applying ideal gates to $\rho_{\text{th}}$. The experiments

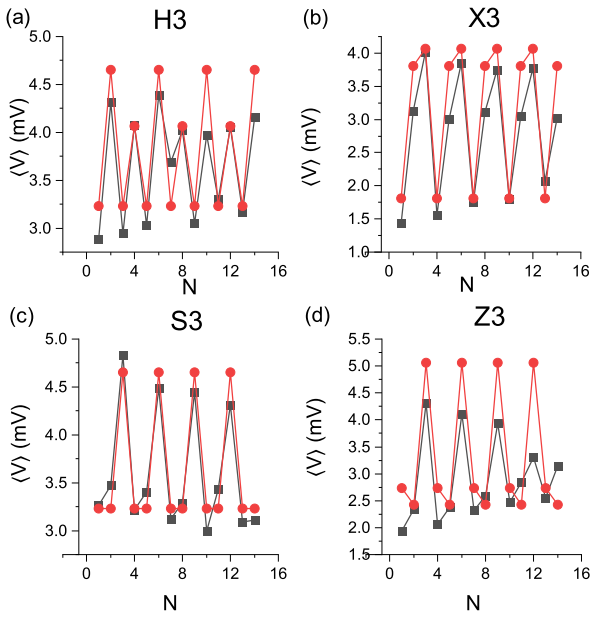


Figure 3.3: $\langle V \rangle$ versus $N$ for repeated applications of $H3$, $X3$, $S3$, and $Z3$, shown in panels (a), (b), (c), and (d) respectively. The red circles are the expected $\langle V \rangle$ versus $N$ signal for the ideal gate, and the black squares are the experiment results.

confirm the expected periodicity of these elements of the Clifford group. The deviation from the expected result increases with $N$, due to errors in control and decoherence.

We now discuss the sources of error in the experiment. Comparing results from the RB and QPT experiment, the individual gate fidelities found in QPT are comparable to the average gate fidelity from RB. In the RB experiment, $V_i = 5.36 \pm 0.03\,\mathrm{mV}$ matches $\mathrm{tr}\,(V\rho_{\mathrm{th}}) = 5.35 \pm 0.07\,\mathrm{mV}$ and $V_f = 4.50 \pm 0.07\,\mathrm{mV}$ matches $\mathrm{tr}\,(V\rho_{\mathrm{dep}}) = 4.59 \pm 0.03\,\mathrm{mV}$, where $\rho_{\mathrm{dep}} = \frac{1}{3}(|0\rangle\langle 0| + |1\rangle\langle 1| + |2\rangle\langle 2|)$. This is consistent with the RB sequence behaving as a depolarizing channel [46]. Numerical simulations of the time dynamics of the system are done in a first step without including decoherence. The Hamiltonian is truncated to the seven lowest energy states, which was found to be sufficient to properly explain level shifts in previous work including two-photon driving (See Section 3.4 and Ref. [11]). Figure 3.2 (a) compares the results (Simulation 1) with experiments. The simulation fit gives $\bar{\mathcal{F}} = 98.3 \pm 0.4\%$, which is close to the experimental result. Simulations also show a drop in fidelity when increasing $\Omega_{01}$ and $\Omega_{12}$, as well as a weak variation when scaling the drive voltage, as observed in the experiment. Numerical simulation of each gate in $\mathcal{C}_3$

individually, and then averaging their respective fidelities, gave $\bar{\mathcal{F}} = 98.4 \pm 1.08\%$, with individual gate fidelities ranging from 95.8% to 99.9%. This shows that in addition to the average fidelity being high, each gate in $\mathcal{C}_3$ is synthesized to high fidelity as well. The range in fidelity is also comparable to the range of fidelities from QPT.

From numerical simulations, we calculate the baseline of the exponential decay to be $V_f = 4.00 \pm 0.09\,\mathrm{mV}$, with error accounting for the experimental errors in $P_{\mathrm{th},1}$ and the readout voltage levels $V_0$, $V_1$, and $V_2$. This value is significantly lower than $V_f$ from the RB data fit and the expected value $V_f = \mathrm{tr}\,(V\rho_{\mathrm{dep}})$. A likely cause for this is leakage out of the qutrit space $\mathrm{span}(\{|0\rangle, |1\rangle, |2\rangle\})$. Figure 3.2 (b) shows the populations based on the simulation. These populations are used to determine the leakage $L_1$ per Clifford gate, the seepage $L_2$, and the adjusted average fidelity $\bar{\mathcal{F}}_L$ following [3]. Whereas leakage measures population transfer out of the qutrit space, seepage measures population transfer into the qutrit space. Simulation 1 gives $L_1 = (1.36 \pm 0.82) \times 10^{-3}$, $L_2 = (6.50 \pm 2.83) \times 10^{-3}$, and $\bar{\mathcal{F}}_L = 96.9 \pm 1.4\%$. Since $\bar{\mathcal{F}}_L$ is not significantly smaller than the simulated $\bar{\mathcal{F}}$, and the small leakage approximation from Ref. [3] matches the simulated populations, leakage does not contribute significantly to the error in simulation.

To gain further insight into the role of leakage in the experiment, we modeled the measured homodyne voltage with additional components arising from higher states (Simulation 2 in Fig. 3.2 (a)). The only significant populations of higher states are those for states $|3\rangle$ and $|6\rangle$, which arises due to the strength of matrix elements in the driving Hamiltonian. We analyzed the measured $\langle V\rangle$ vs $l$ RB data in terms of a model where $\langle V\rangle = \sum_{n=0}^{6} V_n P_n$, with the populations $P_n$ based on the simulations and $V_3$ and $V_6$ as free parameters. The resulting $V_3 = 4.69 \pm 1.15\,\mathrm{mV}$ and $V_6 = 6.89 \pm 1.83\,\mathrm{mV}$ give $V_i = 5.37 \pm 0.03\,\mathrm{mV}$ and $V_f = 4.51 \pm 0.12\,\mathrm{mV}$, in line with experimental values. However the decay constant of the curve disagrees with the experiment. The uncertainty in the estimated $V_3$ and $V_6$ is also much larger than the experimentally-measured uncertainty of the readout voltages for the states in the qutrit space, suggesting that non-zero $V_3$ and $V_6$ is not the primary contributor to RB experiment error.

The role of decoherence is analyzed using a model that includes measured relaxation and excitation rates and dephasing in the qutrit space. Simulation 3 in Fig. 3.2 (a) show numerical results with a model that includes decoherence but neglects the contribution of states outside the qutrit space to $\langle V\rangle$. Adding decoherence to the simulations brings the range of measured $\langle V\rangle$ for a given $l$ in line with experiment values, and gives a $V_f$ of $4.17 \pm 0.04\,\mathrm{mV}$. This indicates that decoherence further reduces the dependence of $\bar{\mathcal{F}}$ on spurious occupation of higher levels. Based on these results, we conclude that contributions to the error from leakage and decoherence are therefore small compared to coherent control

errors.

To analyze coherent control error in the qutrit RB experiment, the errors of Clifford group unitaries must be connected to errors in their component $R(\theta)_{\phi}^{mn}$. For a noisy implementation $\tilde{C} = \prod_n \tilde{R}_n$ of a qutrit gate $C = \prod_n R_n$, with $\tilde{R}_n$ of noisy versions of ideal Givens rotations $R_n$, the gate error $r(\tilde{C}, C) = 1 - \mathcal{F}(\tilde{C}, C)$ is approximately $r(\tilde{C}, C) \approx \sum_n r(\tilde{R}_n, R_n)$, with $r(\tilde{R}_n, R_n)$ the error for a Givens rotation. The approximation follows from modeling the error for a Givens rotation as an operator $K_n = \tilde{R}_n R_n^{\dagger}$, with $K_n = \alpha_n I + \beta_n M_n$, where $\alpha_n$ the complex number minimizing $||K_n - \alpha_n I||_{\infty}$, $\beta_n = ||K - \alpha I_n||_{\infty}$, and $M_n = \frac{1}{\beta_n}(K_n - \alpha_n I)$. $||A||_{\infty}$ is the magnitude of the largest eigenvalue for an operator $A$. Relating $\alpha_n$ and $\beta_n$ to $\mathcal{F}(\tilde{R}_n, R_n)$ and $\mathcal{F}(\tilde{C}, C)$ using

$$\mathcal{F}(\tilde{V}, V) = \frac{\sum_{U_j \in \mathcal{P}_d} \mathrm{tr}\left(V^{\dagger} U_j V \tilde{V} U_j \tilde{V}^{\dagger}\right) + d^2}{d^2(d+1)} \tag{3.2}$$

for two unitaries $V$ and $\tilde{V}$ yields $r(\tilde{C}, C) \approx \sum_n r(\tilde{R}_n, R_n)$, assuming products of $\beta_n$ are small. (See Section 3.6) Figure 3.4 (a) shows that the approximation holds numerically, and gets better as $r(\tilde{C}, C)$ decreases.

To understand the errors in individual Givens rotations, the effective Hamiltonian $H_{\text{eff}} = -\frac{i}{\tau} \ln \tilde{R}_n$ is calculated for each numerically calculated $\tilde{R}_n$, where $\tau$ is the effective time to implement $R_n$ and $\ln \tilde{R}_n$ is the matrix logarithm. The difference between $H_{\text{eff}}$ and the ideal control Hamiltonian $H_{\text{drive}}$ can be connected to errors introduced by the failure of the rotating wave approximation. Figure 3.4 (b) shows the error of the Givens rotations versus drive strength, showing that the error scales quadratically with the drive strength. The effective Hamiltonian is well-approximated by $H_{\text{drive}} + s_{mn}\Omega_{mn}^2 \sigma_z^{mn}$, with $\sigma_z^{mn} = |m\rangle\langle m| - |n\rangle\langle n|$. The coefficients $s_{mn}$ are well-approximated by $s_{mn} = \frac{1}{2(\omega_{mn} - \omega_d)}$, where $\omega_d$ is the drive frequency. These results indicate that the main errors are caused by driving-induced level shifts. Figure 3.4 (c) shows $\mathrm{tr}\,(H_{\text{eff}}\sigma_z^{mn})$ for $mn = 01$ and $mn = 12$ for $R(\pi)_0^{01}$ and Figure 3.4 (d) shows the results for $R(\pi)_0^{12}$. The leakage error identified in the RB analysis is also visible in simulation of the Givens rotations as non-negligible values of $\langle 2|H_{\text{eff}}|3\rangle$, $\langle 1|H_{\text{eff}}|6\rangle$, and $\langle 2|H_{\text{eff}}|6\rangle$. However, these terms are small compared to $\mathrm{tr}\,(H_{\text{eff}}\sigma_z^{mn})$, confirming that contribution of leakage to the control error is small compared to level shifts. Note that level shift errors are much more significant for qutrit control than for qubit control, since the level shift is a coherent error on levels used to store information in qutrits, compared to an incoherent error on levels not used to store information in qubits.

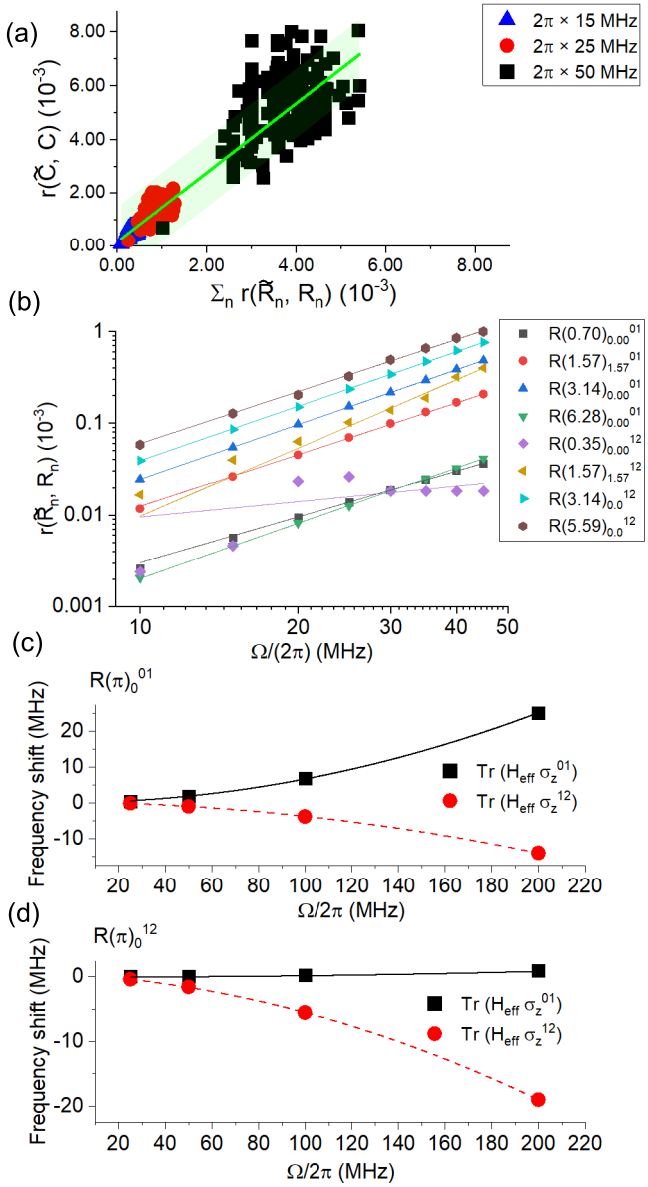


Figure 3.4: (a) The error of the Clifford gate versus the sum of the errors of the component Givens rotations for $\mathcal{C}_3$ at various drive frequencies. The line of best fit and 95% prediction bands are also shown. (b) The error versus the drive frequency for a set of Givens rotations, at $\Omega = 2\pi \times 50$ MHz. The Stark shift and Bloch-Siegert Shift shown for (c) $R(\pi)_0^{01}$ and for (d) $R(\pi)_0^{12}$. The lines in (c) and (d) show quadratic fits.

In conclusion, we have demonstrated control sufficient to synthesize the qutrit Clifford group $\mathcal{C}_3$ to 99% fidelity, using a universal method for gate decomposition into Givens rotations. While leakage out of the qutrit space and decoherence contribute to the measured gate errors, level shifts due to off resonant coupling to states outside the driven two-dimensional subspace corresponding to each Givens rotation are the dominant source of error. In future work it will be important to explore application of level shift corrections, as done in Ref. [11], and more generally design optimal control pulses that mitigate both level shifts and leakage. These results establish randomized benchmarking as a tool to understand superconducting qutrit control and pave the way towards using superconducting qudits in quantum information tasks.

## 3.2 Experiment Details

The device is manufactured using a planar process described in Ref. [11]. The device is capacitively coupled to a coplanar waveguide resonator for dispersive readout, and to a transmission line terminated by a capacitor for control. The device is placed in a microwave package and mounted in a dilution croystat. Experiments are done with the device operated at its flux symmetry point, with the required flux provided by an external coil. The measured transition frequencies are $\omega_{01} = 2\pi \times 1.15\,\mathrm{GHz}$, $\omega_{12} = 2\pi \times 5.69\,\mathrm{GHz}$, and $\omega_{23} = 2\pi \times 5.12\,\mathrm{GHz}$, where $\omega_{mn}$ is the frequency of the transition between states $m$ and $n$. The Rabi frequency has the expected linear dependence on applied ac voltage for each transition, with a slope of $1021 \pm 4\,\mathrm{MHz}$ ($411 \pm 4\,\mathrm{MHz}$) for the 01 (12) transition. Readout is done with a resonator of resonance frequency $2\pi \times 6.72\,\mathrm{GHz}$ and full-width at half-maximum (FWHM) of $2\pi \times 784\,\mathrm{kHz}$, coupling to the lowest two levels of the device with a Jaynes-Cummings interaction strength of $g_{01} = 2\pi \times 11.6\,\mathrm{MHz}$.

The population of the first excited state in the thermal state $\rho_{\mathrm{th}}$ is measured by comparing the amplitude of two Rabi oscillations between $|0\rangle$ and $|1\rangle$. The first oscillation is done starting with the thermal state with populations in states $|1\rangle$ and $|2\rangle$ swapped, and the second oscillation is done starting with the thermal state with a $|0\rangle - |1\rangle$ population swap followed by a $|1\rangle - |2\rangle$ swap prior to performing the Rabi oscillation. The voltage levels $V_0$, $V_1$, and $V_2$ in the readout voltage observable $V$ are characterized by measuring $\langle V \rangle$ for three reference states: the thermal state, the thermal state followed by swapping states $|0\rangle$ and $|1\rangle$, and the thermal state followed by swapping states $|1\rangle$ and $|2\rangle$, then swapping states $|0\rangle$ and $|1\rangle$ [10]. From these measurements, $\rho_{\mathrm{th}} = (0.703 \pm 0.007)\,|0\rangle\langle 0| + (0.297 \pm 0.007)\,|1\rangle\langle 1|$, $V_0 = 6.57 \pm 0.06\,\mathrm{mV}$, $V_1 = 2.47 \pm 0.03\,\mathrm{mV}$, and $V_2 = 4.73 \pm 0.05\,\mathrm{mV}$. The ground state population of the thermal state $\langle 0|\rho_{\mathrm{th}}|0\rangle$ is consistent with an effective temperature of

Table 3.1: The decoherence rates measured in the qutrit space.

| Rate | Value (Hz) |
|---|---|
| $\Gamma_1^{10}$ | $1.62 \times 10^4$ |
| $\Gamma_1^{01}$ | $5.40 \times 10^3$ |
| $\Gamma_1^{21}$ | $3.15 \times 10^5$ |
| $\Gamma_1^{12}$ | $1.50 \times 10^4$ |
| $\Gamma_1^{20}$ | $2.16 \times 10^4$ |
| $\Gamma_1^{02}$ | $1.50 \times 10^3$ |
| $\Gamma_2^{01}$ | $2.04 \times 10^5$ |
| $\Gamma_2^{12}$ | $2.38 \times 10^5$ |
| $\Gamma_2^{02}$ | $1.82 \times 10^5$ |

$64 \pm 2\,\mathrm{mK}$.

We extract the coherence times of the device used as a qutrit following Ref. [10]. Table 3.1 shows the relaxation ($m > n$) and excitation ($m < n$) rates $\Gamma_1^{mn}$ and the Ramsey dephasing rates $\Gamma_2^{mn}$ for all pairs of the qutrit energy levels [24, Sec. 2.7].

## 3.3 The Gate Decomposition

The gate decomposition, based on Ref. [44], decomposes a qutrit gate $U$ into a product of up to nine Givens rotations $R(\theta)_\phi^{mn}$, where $\theta$ is the rotation angle, $\phi$ is the rotation phase, and $mn$ is the two dimensional subspace on which this rotation acts. The first step consists of finding three rotations $R(\theta_1)_{\phi_1}^{01}$, $R(\theta_2)_{\phi_2}^{12}$, and $R(\theta_3)_{\phi_3}^{01}$, which, when applied in sequence, transform $U$ into a diagonal form. For $R(\theta_1)_{\phi_1}^{01}$, setting $\theta_1$ and $\phi_1$ via

$$\sin\theta_1 = \frac{|\langle 0|U|2\rangle|}{\sqrt{|\langle 0|U|2\rangle|^2 + |\langle 1|U|2\rangle|^2}} \tag{3.3}$$

and

$$e^{i\phi_1} = i\frac{(\langle 0|U|2\rangle)^\dagger \langle 1|U|2\rangle}{|\langle 0|U|2\rangle|\,|\langle 1|U|2\rangle|}, \tag{3.4}$$

and applying $R(\theta_1)_{\phi_1}^{01}$ to $U$ yields a $U'$ with $\langle 0|U'|2\rangle = 0$. Continuing in the sequence, $R(\theta_2)$ leads to cancellation of $\langle 1|U'|2\rangle$ to give $U''$, which is $U'$ after applying $R(\theta_2)_{\phi_2}^{12}$, $R(\theta_3)$ leads to cancellation of $\langle 0|U''|1\rangle$ to give a unitary $U_{\mathrm{diag}}$, which has no off-diagonal elements.

Table 3.2: The Givens Rotation decompositions for $H_3$, $S_3$, $X_3$, and $Z_3$.

| Pulse Number | $H_3$ | $S_3$ | $X_3$ | $Z_3$ |
|---|---|---|---|---|
| 0 | $R(1.5708)^{01}_{2.61799}$ | $R(1.5708)^{01}_{1.5708}$ | $R(3.14159)^{12}_{0.0}$ | $R(1.5708)^{12}_{1.5708}$ |
| 1 | $R(1.91063)^{12}_{-3.66519}$ | $R(1.39626)^{01}_{-3.14159}$ | $R(3.14159)^{01}_{0.0}$ | $R(4.18879)^{12}_{0.0}$ |
| 2 | $R(1.5708)^{01}_{1.0472}$ | $R(1.5708)^{01}_{-1.5708}$ | $R(1.5708)^{01}_{1.5708}$ | $R(1.5708)^{12}_{-1.5708}$ |
| 3 | $R(1.5708)^{01}_{1.5708}$ | $R(1.5708)^{12}_{1.5708}$ | $R(6.28319)^{01}_{-3.14159}$ | |
| 4 | $R(4.18879)^{01}_{-3.14159}$ | $R(2.79253)^{12}_{-3.14159}$ | $R(1.5708)^{01}_{-1.5708}$ | |
| 5 | $R(1.5708)^{01}_{-1.5708}$ | $R(1.5708)^{12}_{-1.5708}$ | $R(1.5708)^{12}_{1.5708}$ | |
| 6 | $R(1.5708)^{12}_{1.5708}$ | | $R(3.14159)^{12}_{-3.14159}$ | |
| 7 | $R(1.0472)^{12}_{-3.14159}$ | | $R(1.5708)^{12}_{-1.5708}$ | |
| 8 | $R(1.5708)^{12}_{-1.5708}$ | | | |

The second step implements the diagonal elements of $U_{\text{diag}}$. For a qutrit gate, this requires two phase gates, each of which has the form

$$\exp\left(i\beta\sigma_z^{mn}\right) = R\left(\frac{\pi}{2}\right)^{mn}_{\frac{\pi}{2}} R(2\beta)^{mn}_0 R\left(\frac{\pi}{2}\right)^{mn}_{-\frac{\pi}{2}}, \tag{3.5}$$

where $\sigma_z^{mn} = |m\rangle\langle m| - |n\rangle\langle n|$. A total of six rotations are needed in this step, with the first three rotations implementing a $|0\rangle - |1\rangle$ phase gate, and the last three rotations implementing a $|1\rangle - |2\rangle$ phase gate.

Each $R(\theta)^{mn}_{\phi}$ is mapped to a single microwave control pulse with a cosine rise and fall envelope with $t_{\text{rise}} = t_{\text{fall}} = 2\,\text{ns}$, and the pulse amplitude determined by the drive strength $\Omega_{mn}$. The pulse duration is constrained to be at least $t_{\text{rise}} + t_{\text{fall}}$, which requires the drive strength for a pulse to be reduced if a rotation of $\theta$ cannot be implemented at the drive strength $\Omega_{mn}$. Figure 3.5 gives the AWG waveforms implementing the gates $H_3$, $S_3$, $X_3$, and $Z_3$ using the decomposition presented above, at a drive strength $\Omega_{01} = \Omega_{12} = 2\pi \times 50\,\text{MHz}$. Table 3.2 gives the Givens rotation decomposition for these gates. The waveforms in Figure 3.5 implement the pulses shown in Table 3.2.

Following Ref. [44], generalizing the decomposition from qutrit gates to a $d$-dimensional qudit gate $U$ requires a total of $\frac{1}{2}d(d-1)$ rotations are needed in the first step of the decomposition, equal to the number of elements of $U$ in the upper-triangular region. In the second step, the $d-1$ phase gates required to implement the diagonals of $U$ require $3(d-1)$ rotations to implement. The total number of rotations required to implement $U$ is therefore of order $O(d^2)$.

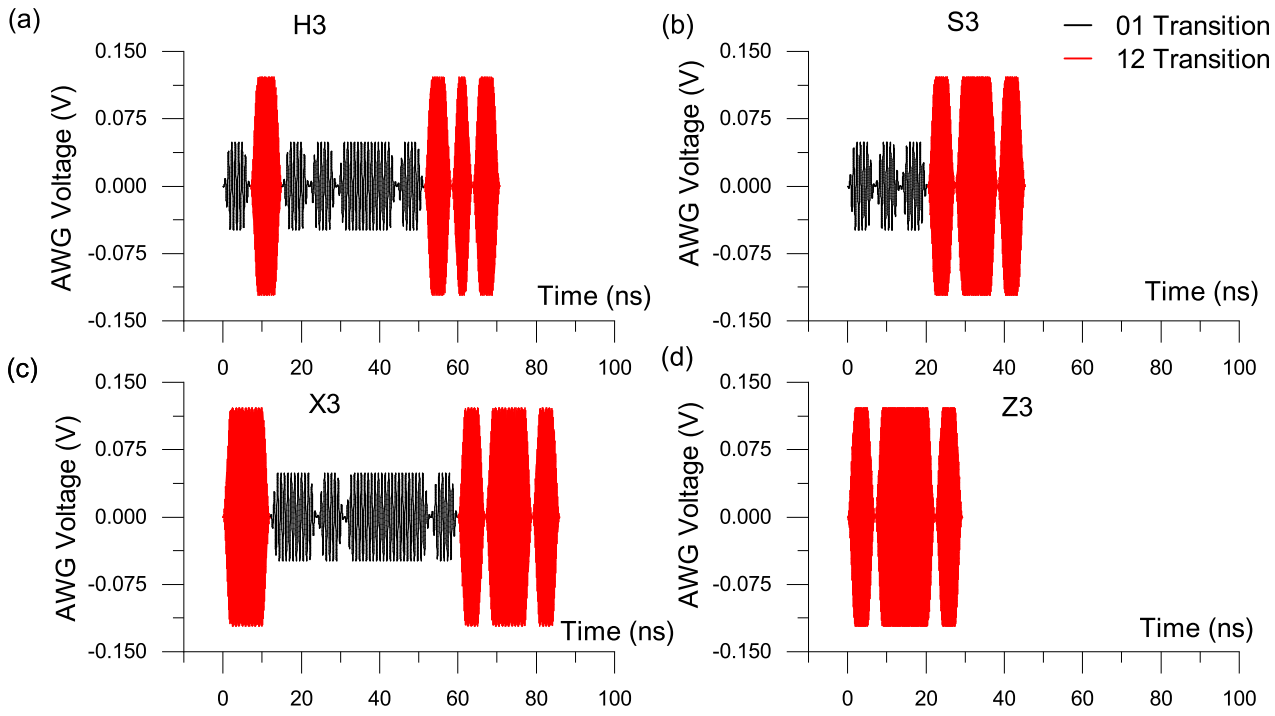


Figure 3.5: The waveforms implementing the qutrit gates $H_3$ (a), $S_3$ (b), $X_3$ (c), and $Z_3$ (d). Black (dark) areas indicate 01 transitions and red (light) areas indicate 12 transitions.

Table 3.3: The coefficients of $H_{\text{static}}$ used in simulations. All other coefficients not shown are zero.

| Coefficient | Value ($2\pi \times 10^9$ Hz) |
|---|---|
| $\omega_{01}$ | 1.146 |
| $\omega_{02}$ | 6.838 |
| $\omega_{03}$ | 11.96 |
| $\omega_{04}$ | 17.22 |
| $\omega_{05}$ | 17.78 |
| $\omega_{06}$ | 18.34 |

## 3.4 Numerical Simulation of Device Dynamics

The circuit Hamiltonian, derived in the model presented in Ref. [10], together with the drive has the form $H(V(t)) = H_{\text{static}} + H_{\text{drive}}(V(t))$, where $H_{\text{static}} = \sum_{j=1}^{s-1} \omega_{0j} |j\rangle\langle j|$ and $H_{\text{drive}}(V(t)) = \sum_{\substack{i,j=0 \\ i \neq j}}^{s-1} V(t)(g_{ij}|i\rangle\langle j| + \text{h.c.})$ describes time-dependent control with the voltage $V(t)$ at control pad of the device. The Hilbert space is truncated to the lowest $s = 7$ levels, owing to the agreement between the simulation and previous multi-level control experiments including two-photon Rabi oscillations [11]. The transition frequencies $\omega_{0j}$ and the transition matrix elements $g_{ij}$ of the voltage operator are calculated from the circuit model fitted to experiment data. Table 3.3 gives the values of $\omega_{0j}$ and Table 3.4 gives the values of $g_{ij}$ used in the simulation.

The decoherence model consists of Lindblad operators of the form $\sqrt{\Gamma_1^{mn}}\,|m\rangle\langle n|$ for relaxation/excitation, and $\sqrt{\frac{1}{2}\Gamma_2^{mn}}(|m\rangle\langle m| - |n\rangle\langle n|)$ for dephasing. To determine $\rho(t)$ after applying an RB sequence, the Lindblad master equation [5, Sec. 8.4.1] is solved numerically in qutip [48]. One solution is found with $|0\rangle\langle 0|$ as the initial state, another is found with $|1\rangle\langle 1|$ as the initial state, and $\rho(t)$ is determined by combining the two solutions together. $\langle V \rangle$ is determined by $\text{tr}\,(V\rho(t))$. This approach propagates measured uncertainties in $P_{\text{th},0}$ and uncertainties in the elements of $V$. For numerical simulations of Clifford gates and Givens rotations, the corresponding propagator at the end of the decomposition of the gate is calculated, and compared against the ideal propagator. The AWG waveform voltage is related to the voltage at the device control pad $V(t)$ by scaling the voltage of 01 and 12 pulses by their respective transfer coefficients $c_{01} = 5.84 \times 10^{-3}$ and $c_{12} = 7.02 \times 10^{-4}$. These coefficients are determined by simulating a Rabi experiment, and matching the Rabi frequency with the experimentally-measured value.

Table 3.4: The coefficients of $H_{\text{drive}}$ used in simulations. All other coefficients not shown are zero.

| Coefficient | Value ($2\pi \times 10^9\,\text{Hz}\,\text{V}^{-1}$) |
|---|---|
| $g_{01}$ | $174.7$ |
| $g_{03}$ | $-294.2 + 205.2i$ |
| $g_{04}$ | $105.6 + 32.43i$ |
| $g_{12}$ | $584.6$ |
| $g_{15}$ | $90.71 + 65.45i$ |
| $g_{16}$ | $-119.7 - 223.2i$ |
| $g_{23}$ | $567.5 - 395.9i$ |
| $g_{24}$ | $-17.72 - 5.442i$ |
| $g_{35}$ | $-4.953 - 14.15i$ |
| $g_{36}$ | $-109.6 + 931.7i$ |
| $g_{45}$ | $93.17 + 31.61i$ |
| $g_{46}$ | $0.2782 + 0.2757i$ |

## 3.5 Calculation of Gate Fidelity

Following [28], the gate fidelity $\mathcal{F}(\tilde{\mathcal{U}}, U)$, where $\tilde{\mathcal{U}}$ is a noisy implementation of $U$, is

$$\mathcal{F}(\tilde{\mathcal{U}}, U) = \frac{1}{d^2(d+1)} \sum_{P \in \mathcal{P}_d} \text{tr}\left(P^\dagger U^\dagger \tilde{\mathcal{U}}(P) U\right) + \frac{1}{d+1}, \tag{3.6}$$

where $\mathcal{P}_d$ is the Pauli group defined on a $d$-dimensional Hilbert space [47]. Since the device simulation is conducted over seven dimensions, but the RB experiment is conducted over three dimensions, it is necessary to find the gate fidelity averaged over a subspace of states considered in the simulation, to obtain a gate fidelity comparable to the RB experiment. To find the gate fidelity for the qutrit subspace, the elements of $\mathcal{P}_3$ are expanded into 7-dimensional operators by padding the matrices with zeroes such that $P \in \mathcal{P}_3$ occupied the top-left $3 \times 3$ block. $\mathcal{F}(\tilde{\mathcal{U}}, U)$ is then found using equation 3.6 with $d = 3$. This is done because the elements of $\mathcal{P}_3$ are used as a basis for writing down the maximally-entangled qutrit state $|\phi\rangle = \frac{1}{\sqrt{3}}(|0\rangle|0\rangle + |1\rangle|1\rangle + |2\rangle|2\rangle)$. $\mathcal{F}(\tilde{\mathcal{U}}, U)$ is related, and ultimately derived from, the entanglement fidelity $F_e(U^\dagger \circ \tilde{\mathcal{U}}) = \langle\phi| I_3 \otimes (U^\dagger \circ \tilde{\mathcal{U}})|\phi\rangle$, where $I_3 = |0\rangle\langle 0| + |1\rangle\langle 1| + |2\rangle\langle 2|$, via

$$\mathcal{F}(\tilde{\mathcal{U}}, U) = \frac{dF_e(U^\dagger \circ \tilde{\mathcal{U}}) + 1}{d+1}, \tag{3.7}$$

following Ref. [28]. Since the qutrit maximally entangled state has no components outside the lowest three levels, the elements of $\mathcal{P}_3$ cannot have support outside the space spanned by the lowest three levels, meaning $\mathcal{P}_3$ elements expand by padding with zeroes. This also means $\mathcal{P}_3$ elements that are unitary in 3 dimensions are not unitary in 7 dimensions.

## 3.6 Approximating the Fidelity of Clifford Gates from Givens Rotations

Let $C$ represent an ideal Clifford gate and $\tilde{C}$ represent its error-prone implementation. $\tilde{C}$ is $\prod_n \tilde{R}_n$, where $\tilde{R}_n = K_n G_n$ is a noisy implementation of an ideal Givens rotation $R_n$ with error $K_n$. Assume $K_n = \alpha_n I + \beta_n M_n$, where $\alpha_n \in \mathbb{C}$, $\beta \in \mathbb{R}$, $M_n$ is an operator, and $I$ is the identity operator. $\alpha_n$ is the complex number minimizing the magnitude of the largest eigenvalue of $K_n - \alpha_n I$, denoted $||K_n - \alpha_n I||_\infty$. $\beta_n = ||K_n - \alpha_n I||_\infty$ and $M_n = \frac{1}{\beta_n}(K_n - \alpha_n I)$. The zeroth-order approximation to the fidelity $\mathcal{F}_0(\tilde{C}, C)$ assumes $\beta_n$ is negligible. The fidelity then simplifies as

$$\mathcal{F}_0(\tilde{C}, C) = \mathcal{F}\left(\prod_n K_n R_n, \prod_n R_n\right)\Big|_{\beta_n=0} \tag{3.8}$$

$$= \mathcal{F}_0\left(\prod_n \alpha_n \prod_n R_n, \prod_n R_n\right) \tag{3.9}$$

$$= \mathcal{F}_0\left(\prod_n \alpha_n I, I\right) \tag{3.10}$$

$$= \frac{1}{d^2(d+1)} \sum_j \mathrm{tr}\left(\left(\prod_n \alpha_n U_j \prod_n \alpha_n^* U_j^\dagger\right)\right) + \frac{1}{d+1} \tag{3.11}$$

$$= \frac{1}{d^2(d+1)} \prod_n |\alpha_n|^2 \sum_{j=1}^{d^2} \mathrm{tr}\left(U_j U_j^\dagger\right) + \frac{1}{d+1} \tag{3.12}$$

$$= \frac{1}{d^2(d+1)} \prod_n |\alpha_n|^2 \sum_{j=1}^{d^2} \mathrm{tr}\left(I_3\right) + \frac{1}{d+1} \tag{3.13}$$

$$= \frac{d\prod_n |\alpha_n|^2 + 1}{d+1}. \tag{3.14}$$

Let $r_0(\tilde{C}, C) = 1 - \mathcal{F}_0(\tilde{C}, C)$ represent the zeroth-order approximation to the error. For a single Givens rotation $\tilde{R}_n$, $\alpha_n$ is related to $r_0(\tilde{R}_n, R_n)$ by

$$|\alpha_n|^2 = 1 - \frac{d+1}{d} r_0(\tilde{R}_n, R_n). \tag{3.15}$$

The zeroth-order error for a Clifford gate is then

$$r_0(\tilde{C}, C) = \left(\frac{d}{d+1}\right)\left(1 - \prod_n \left(1 - \left(\frac{d+1}{d}\right) r_0(\tilde{R}_n, R_n)\right)\right). \tag{3.16}$$

Since $r_0(\tilde{R}_n, R_n)$ is small, one can make the approximation

$$\prod_n \left(1 - \left(\frac{d+1}{d}\right) r_0(\tilde{R}_n, R_n)\right) \approx 1 - \left(\frac{d+1}{d}\right) \sum_n r_0(\tilde{R}_n, R_n), \tag{3.17}$$

giving $r_0(\tilde{C}, C) \approx \sum_n r_0(\tilde{R}_n, \tilde{R}_n)$. If $\beta$ is small, then $r(\tilde{C}, C) \approx \sum_n r(\tilde{R}_n, R_n)$.

To get a more accurate approximation to $r(\tilde{C}, C)$, consider a $\tilde{C}$ made of two Givens rotations, such that $\tilde{C} = K_2 R_2 K_1 R_1$. To get the first-order approximation to the fidelity $\mathcal{F}_1(\tilde{C}, C)$, assume any terms with more than one $\beta$ are negligible when taking the product $U_j^\dagger C^\dagger \tilde{C} U_j \tilde{C}^\dagger C$. The approximation is

$$U_j^\dagger C^\dagger \tilde{C} U_j \tilde{C}^\dagger C \approx \alpha_2 \alpha_1 \alpha_1^* \alpha_2^* \left(I + U_j^\dagger R_1^\dagger R_2^\dagger \frac{\beta_2 M_2}{\alpha_2} R_2 R_1 U_j + U_j^\dagger R_1^\dagger \frac{\beta_1 M_1}{\alpha_1} R_1 U_j + I_3 \frac{\beta_1 M_1^\dagger}{\alpha_1^*} + I_3 R_1^\dagger \frac{\beta_2 M_2^\dagger}{\alpha_2^*} R_1\right). \tag{3.18}$$

Substituting this into equation 3.6 gives

$$\mathcal{F}_1(\tilde{C}, C) = \frac{d \prod_n |\alpha_n|^2 + 1}{d+1} + \frac{\prod_n |\alpha_n|^2}{d+1}\left(\mathrm{tr}\left(\beta_1 \left(\frac{M_1}{\alpha_1} + \frac{M_1^\dagger}{\alpha_1^*}\right) I_3\right) + \mathrm{tr}\left(\beta_2 \left(\frac{M_2}{\alpha_2} + \frac{M_2^\dagger}{\alpha_2^*}\right) I_3\right)\right), \tag{3.19}$$

which generalizes to

$$\mathcal{F}_1(\tilde{C}, C) = \mathcal{F}_0(\tilde{C}, C) + \frac{\prod_n |\alpha_n|^2}{d+1} \sum_n \mathrm{tr}\left(\beta_n \left(\frac{M_n}{\alpha_n} + \frac{M_n^\dagger}{\alpha_n^*}\right) I_3\right) \tag{3.20}$$

Figure 3.6 shows $r(\tilde{C}, C)$ versus $r_0(\tilde{C}, C)$ and $r_1(\tilde{C}, C)$, for the same Clifford gates as in Figure 4 (a) in the main text. The first-order approximation improves the estimate of $\mathcal{F}(\tilde{C}, C)$, as can be seen by the 95% prediction band narrowing.

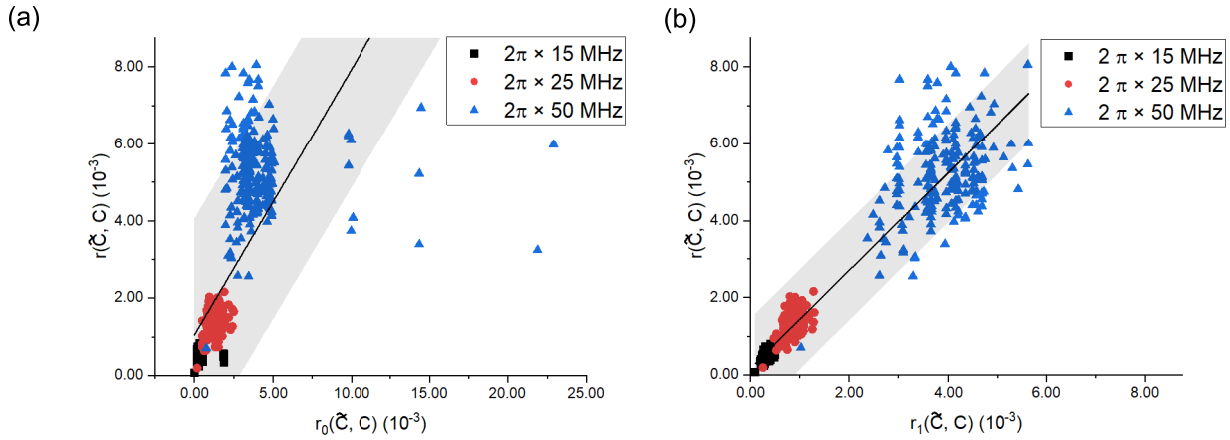


Figure 3.6: The simulated error for each Clifford gate versus its (a) zeroth-order estimate and (b) first-order estimate. The line of best fit and 95% prediction bands are shown as well.

## 3.7 Effective Hamiltonian Calculation

To find the Hamiltonian $H_{\text{eff}}$ such that $U = \exp(-iH_{\text{eff}}\tau)$, the objective function $1 - \mathcal{F}(\mathcal{U}, \exp(-iH_{\text{eff}}\tau))$ is minimized over the space of possible Hamiltonians. In the minimization, the gate fidelity $\mathcal{F}$ is taken over seven dimensions, not three, so that the effective Hamiltonian replicates the dynamics outside the qutrit space as well as inside. The initial condition for this minimization is an ideal Hamiltonian $\tilde{H}$. The Hilbert space of Hamiltonians is parameterized by the Generalized Gell-Mann matrices $G_k$, giving $\tilde{H} = \sum_k \alpha_k G_k$ and $H_{\text{eff}} = \sum_k \beta_k G_k$ [49]. During the minimization, $\beta_k$ is constrained to prevent spurious $2\pi$ rotations from being introduced.

# Chapter 4

# Designing a New Generation of Capacitively-Shunted Flux Qubits

## 4.1 Introduction

The qutrit randomized benchmarking experiment discussed in Chapter 3 establishes the three-pad capacitively-shunted flux qubit (CSFQ) introduced in Section 2.2.2 as a useful device for quantum computing. The fidelity of the qutrit control stands out in particular. The features of the CSFQ that enabled this experiment include its very high anharmonicity and its good coherence time. The anharmonicity of this device offers an advantage over more commonly superconducting qubit implementations like transmons [18]. However, unlike fluxonium devices with similar anharmonicities to the three-pad CSFQ [50], this CSFQ requires only three junctions to work, making manufacturing easier.

A natural next step following the qubit RB experiment is to implement a two-qubit gate using three-pad CSFQ devices. This motivates the new generation of device designs introduced in this chapter. To determine which of the CSFQs should be coupled together to participate in the two-qubit experiment, a set of single CSFQ devices needs to be investigated as well. This set of devices is also necessary to further explore and improve coherence. Section 4.2 of this chapter discusses the single-qubit device design, and section 4.3 discusses how to couple these devices together. Conclusions are drawn in Section 4.4.

## 4.2 Designing Single CSFQ Devices

The qutrit randomized benchmarking (RB) experiment discussed in Chapter 3 identified leakage, lack of knowledge of $V$ for the third excited state and above, and decoherence as sources of error. However, it also showed that high-fidelity qutrit control can be performed on the CSFQ, and that the device is capable of very high anharmonicities. This motivates additional experimental work in CSFQ devices, which requires new CSFQ designs. These designs need to address the low Ramsey coherence time $T_2^*$ (See section 2.4), and the low ground state population observed in the previous experiment.

We first discuss the desired optimizations to make in new CSFQ devices. In the 2020 cooldown when qutrit RB was done, $T_2^*$ ranged from 3.5 $\mu$s to 4.5 $\mu$s. However, $T_{2,\text{echo}}$ from a spin echo experiment [51] was 9.0$\mu$ s, and $T_2$ measured from a Carr-Purcell-Meiboom-Gill (CPMG) experiment [51] was 26.5 $\mu$s. $T_{2,\text{echo}}$ and $T_2$ compare well to values measured in 2018, when the qubit was cooled down for the first time, but $T_2^*$ is much lower [10]. This suggests that there is low-frequency noise in the device, and that driven evolution reduces exposure to this noise.

In addition to the low frequency noise, the thermal ground state population of $0.703 \pm 0.007$ was problematic for state preparation. This population is worse than the 0.95 ground state population observed in the 2018 cooldown. Based on spectroscopy and steady-state population data in 2020, the effective temperature of the device increased to 64 mK. This compares unfavourably to 27 mK measured in 2018 [10]. The low ground state population can be mitigated by increasing the transition frequency. It can also be mitigated by cooling the qubit through Raman scattering to the cavity [11]. This cooling becomes faster as the equilibrium ground state population increases, as less population needs to be transferred from $|1\rangle$ to the readout resonator. Improved state preparation also brings $\rho_{\text{eq}}$ closer in line to RB protocols that assume the device starts in the state $|0\rangle\langle 0|$ [6, p. 18]. This makes protocols like leakage RB [3] more effective.

Finally, it is useful to explore wider parameter ranges in a single cooldown of the device, and have reproducibility checks done consistently. The device on which the RB experiment was conducted only had two qubits on a $7 \times 3$ mm die. Of these, only one was used in qutrit RB since it had a higher transition frequency. Increasing the number of devices per die allows multiple design variations to be investigated in the same cooldown. This reduces variability in devices between cooldowns, increases device density, and improves reproducibility of results. Devices can be distinguished by coupling to readout resonators of different frequency as in [52].

Having outlined the desired optimizations to make in the CSFQ devices, we now discuss

the properties against which CSFQ designs were evaluated. The first such property is the set of the qubit transition frequencies, denoted $\omega_{mn}$. It is useful to have all transition frequencies of interest between 1.5 and 7 GHz. The lower bound ensures a high ground state population in the thermal state, denoted $\langle 0|\rho_{\text{eq}}|0\rangle$. The upper bound avoids collisions between the readout resonator frequency and a transition frequency, which violates the large cavity-qubit detuning required for dispersive readout. The Purcell effect is also more promiment as the qubit frequency gets closer to the readout resonator frequency, reducing qubit coherence [20]. The readout resonator frequencies were chosen to be between 7.1 and 7.7 GHz, in order to comply with an 8 GHz frequency limit on the readout amplifier. It is important to consider two-photon transition frequencies as well as the single-photon transitions. Transition frequencies can be increased by reducing the size of the CSFQ capacitive pads, and increasing the critical current of the Josephson junctions, and reducing the ratio of critical currents between the small and large junctions, denoted $\alpha$.

In addition to the transition frequencies, anharmonicities must be considered as well. Anharmonicity is the difference between $\omega_{12}$ and $\omega_{01}$, and it measures how far the CSFQ deviates from being a harmonic oscillator [53]. Anharmonicity is important as it determines to what extent it is possible to drive the $|0\rangle - |1\rangle$ transition independent of the $|1\rangle - |2\rangle$ transition, and so reduce leakage to $|2\rangle$ when driving the $|0\rangle - |1\rangle$ transition [7, sec. 2.1]. Reducing the drive power reduces the leakage, but this also increases gate time. Techniques to compensate for the additional $|1\rangle$-$|2\rangle$ transition such as DRAG also lose effectiveness as the anharmonicity decreases [53]. In addition to 01 and 12 anharmonicity, it is also necessary to consider the anharmonicity between the 12 and 23 transitions as well, in order to suppress leakage during qutrit control. Anharmonicity can be increased by raising $\alpha$.

The persistent current $I_p$ is the current circulating in the CSFQ in one of the two flux states in the two-level approximation of the CSFQ [9]. It is determined by fitting $\omega_{01}$ to the Hamiltonian

$$H = \frac{\Delta}{2}\sigma_x + \frac{1}{2}I_p\Phi_0\left(f - \frac{1}{2}\right)\sigma_z, \tag{4.1}$$

where $\sigma_x$ and $\sigma_z$ are in the flux state basis. The flux states $|l\rangle$ and $|r\rangle$ are related to $|0\rangle$ and $|1\rangle$ by $|0\rangle = \frac{1}{\sqrt{2}}(|l\rangle + |r\rangle)$ and $|1\rangle = \frac{1}{\sqrt{2}}(|l\rangle - |r\rangle)$ at the symmetry point. A high persistent current results in high susceptibility to flux noise, but some persistent current must be present in the system in order to tune the CSFQ. Furthermore, a low persistent current requires small junctions to be made, placing more demands on the fabrication process and harming reproducibility. In the CSFQ from Chapter 3, $I_p$ was 73.4 nA in 2018, but it increased to 86.4 nA by the time the qutrit RB experiment was conducted in 2020. These values are higher than the design value of 60 nA. Reducing $I_p$ to 40 nA is a goal of this

design.

The flux noise sensitivity is $\frac{I_p^2}{\omega_{01}}$ at the symmetry point. This factor relates a flux fluctuation $\delta\phi$ to a fluctuation in the transition frequency $\delta\omega_{01}$. Fluctuations in $\omega_{01}$ cause the qubit to dephase, and this lowers the $T_2^*$ of the qubit. The flux and transition frequency are related by equation 4.1. The sensitivity is found by analyzing $\omega_{01}$ versus $\phi$ at the bias point. At the symmetry point, the first-order term

$$\frac{\partial\omega_{01}}{\partial\phi} = \frac{I_p^2\left(\phi - \frac{1}{2}\phi_0\right)}{\sqrt{\Delta^2 + \left(I_p\left(\phi - \frac{1}{2}\phi_0\right)\right)^2}} \tag{4.2}$$

vanishes, and the second-order term

$$\frac{\partial^2\omega_{01}}{\partial\phi^2} = \frac{I_p^2}{\Delta}\left(\left(\frac{I_p}{\Delta}\left(\phi - \frac{1}{2}\phi_0\right)\right)^2 + 1\right)^{-\frac{3}{2}} \tag{4.3}$$

becomes $\frac{I_p^2}{\omega_{01}}$ [54]. Lowering this factor is a priority, as flux noise contributes to the low coherence observed in the qutrit RB experiment.

The frequency modulation due to charge noise $\delta f_{ng}$ describes the effect of charge noise on the flux qubit. The charge noise is modelled as additive noise on each island of the CSFQ [18], causing the charge on each island to fluctuate. This causes $p = \hbar n$ to fluctuate. To model these effects, the flux qubit Hamiltonian

$$H = 2e^2(n_i - D_{ik}n_{g,k})C_{ij}^{-1}(n_j - D_{jk}n_{g,j}) - \Phi_0 I_{c,n}\cos\gamma_n \tag{4.4}$$

includes an $n_g$ offset for each operator $n_i$. $e$ is the elementary charge, and $D$ maps $n_g$ from each island $k$ on the qubit (see Section 2.2.2), to $n_i$. $H$ is periodic in $n_g$ with period 1. $\delta f_{ng}$ is the difference in extremes in $\omega_{01}$ caused by adding an $n_g$ to any island in the circuit. Higher capacitances reduce the charge modulation, as in the case of transmon qubits, but this comes at the cost of anharmonicity. To increase coherence, charge modulation should be reduced as much as possible.

We now move from discussing design parameters to the available knobs to control. The first is the critical current $I_c$ of the two large junctions. This impacts both $I_p$ and $\omega_{01}$. It can be changed by changing the junction dimensions, or by changing the critical current density $J_c$. The former is determined by design, and the latter is determined by manufacturing process parameters [55, 56], particularly the pressure at which the insulating oxide layer in the Josephson junction is grown. The goal is to reduce $I_c$ in order to reduce $I_p$. However,

reducing $I_c$ also requires smaller junctions to be made. $I_c$ must therefore be considered as part of a collection of design attributes that determine $I_p$. In addition to $I_c$, the value $\alpha$ sets the critical current of the $\alpha$ junction as $\alpha I_c$. $\alpha$ ranges from 0.5 to 1. A high $\alpha$ qubit is difficult to tune, and also lowers the transition frequency at the qubit symmetry point. Small $\alpha$ qubits are more difficult to manufacture since they require small junctions to be made. This problem becomes worse as $I_c$ decreases. The goal for the current designs is to examine the effect of changes in $\alpha$ on CSFQ properties.

Finally, coupling strengths to the readout resonators and control lines must also be considered in the design process. Large coupling strengths permit faster Rabi drive and larger dispersive shifts, respectively. However, having too large a coupling introduces a decoherence channel, as the qubit loses coherence due to the Purcell effect [57]. The Purcell filter is a means of mitigating this problem on the readout resonator, as it reduces the frequency response of the readout line at the qubit transition frequencies [20].

Having reviewed the design attributes against which CSFQ designs are evaluated, we now consider design parameters. The first set of parameters are the dimensions of the qubit pads. The three dimensions considered were the size of the capacitive pads, the perimeter of the qubit, and the size of the gap between pads. Larger pads increase capacitance, and therefore reduce charge modulation, but they also lower the 01 transition frequency and the anharmonicity. Decreasing the gap size increases the capacitance, but bringing the pads too close increases the electric field between the pads. This increases loss due to the large field interacting with two-level systems in the dielectric [58]. The perimeter of the pads should also be as small as possible, so that there are few regions of high electric field on the pads. This reduces the electric field extending from the aluminum electrodes into lossy silicon, improving coherence [18]. Considering that the previous qubit design was shown to work in experiment, and that the pads are close to square on the current CSFQ design, it was decided to keep the aspect ratio of the pads the same, and scale the pads by a factor $k$.

The next most important dimension is the junction size. In principle, $I_c$ can be can be controlled by varying the thickness of the oxide layer, changing the gap between the junction islands, and by changing the junction width. The oxide thickness is determined by the process, and is the hardest variable to control, owing to the thin layer of oxide and the exponential dependence of the critical current density on the thickness of the oxide layer [55].

The junction length, i.e. the width of the Dolan bridge used to fabricate the junction [59], was not changed from the previous design due to the reliability of fabricating junctions with this gap size. This leaves the junction width as a design parameter, with the junction

width being linearly proportional to the critical current. Varying the junction width to set the critical current was more convenient than varying both gap and junction width, and keeping the junction gap was considered less risky for the fab process. However, this made setting $I_c$ and $\alpha$ more difficult as the difference in junction widths became smaller.

Based on the previous qubit design, the distance between the qubit and readout line was scaled by the geometry scale factor $k$, in order to keep the capacitance, and thus dispersive shift, consistent. The control line distance was also scaled by the geometry scale factor to keep the control coupling consistent. Owing to the use of a common control feedline connected to a 50 $\Omega$ load, the predicted Rabi frequency is half that of the previous CSFQ design. This is because since the feedline is not terminated by an open circuit, as in the case of the previous design, an equivalent voltage applied to the control feedline will produce half the voltage at the end of the qubit control line. The length of the coupler between readout resonators and the readout feedline was set to ensure a coupling quality factor $Q$ of $1.7 \times 10^5$, matching the previous qubit design. The coupling $Q$ is the ratio of a resonator frequency to its bandwidth [60, sec. 6.1], and is inversely-proportional to the amount of loss in the resonator.

Finally, the last design parameter varied in the study was the width of the Josephson junction traces. Wider traces have been shown to decrease flux noise, as the magnetic field is spread across multiple wires [61].

To investigate the relation between the design parameters and the design attributes, simulations in ANSYS Q3D and SONNET EM suite were used to model the qubit capacitances, and microwave line frequency responses, respectively. Mathematica code was used to investigate the qubit Hamiltonian. The first step was to determine the capacitances in the single-qubit design as a function of the scale factor. To do this, a finite element simulation in ANSYS Q3D Extractor was set up, and the capacitance matrix was extracted from these islands. In this study, $k$ ranged from 0.5 to 1.5 in increments of 0.1. The lower bound was chosen to prevent dielectric loss from the plates from being significant, and the upper bound was selected to investigate larger capacitive pads while still keeping $\omega_{01}$ large. Values in between were interpolated from simulation data.

In addition to studying the impact of $k$ on pad capacitances, the capacitances between the CSFQ, the bias line, and the drive line were checked in Q3D as well. It was expected that the capacitance between qubit pads and the control antenna would be the same regardless of whether the control antenna was terminated by the edge of the simulation, or whether the antenna connected to a control line. Figure 4.1 labels the control line and control antenna. The Q3D simulation showed that a distance of 175 $\mu$m between the start of the turn in the control line, and the base of the rectangular region was sufficient to

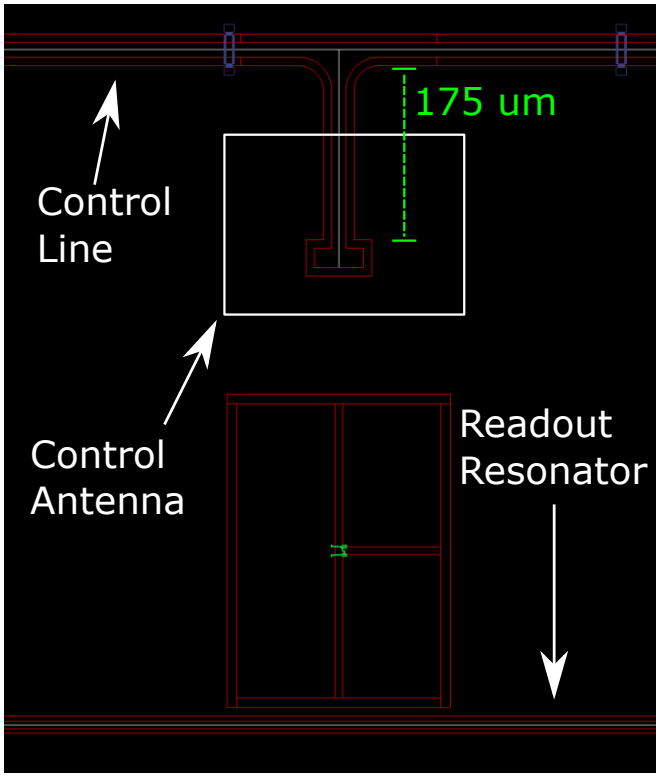


Figure 4.1: An illustration labelling the control antenna, control line, and readout resonator connections for a single qubit. The labelled dimension shows the 175 $\mu$m distance required to isolated the control line from the qubit

isolate the control line from the qubit. The control is therefore expected to behave as in the 2018 design.

The capacitance data as a function of geometry was then inputted into a Mathematica simulation. Given this, and the junction areas, the simulation numerically determined the device Hamiltonian. For scale factors of 0.6, 0.8, 1.0, and 1.2, the design attributes were plotted as a function of the critical current and alpha. The Mathematica simulations showed that there was a region around $I_c = 140$ nA and $\alpha = 0.5$ with good 01 and 12 anharmonicities. However, the region was risky in terms of low transition frequencies and sensitivity of parameters to critical current. The simulations also showed that charge modulation is exponentially suppressed as critical current increases. $\alpha$ was varied by 0.07 between qubit variations, and $I_c$ was varied by 40 nA between qubit variations. This ensures that the resulting junction dimensions vary enough to be writeable by electron

beam lithography. Figure 4.2 shows the design parameters plotted against $I_c$ and $\alpha$. Figure 4.6 (a) and 4.6 (e) shows a difference between $\omega_{23}$ and $\omega_{12}$ of 1.0 GHz at $I_c = 140$nA and $\alpha = 0.55$. When combined with the high anharmonicity seen in Figure 4.2 (c), this merits setting $I_c$ and $\alpha$ to these values, in order to improve qutrit RB.

Finally, SONNET simulations were conducted on parts of the device to determine the microwave frequency response. The devices were modelled using thin lossless metal, with 500 $\mu$m of silicon under the metal, and a ground plane under the silicon. The silicon thickness matches that of the wafer used in fabrication. A 1800 $\mu$m thick air box was placed above the waveguide. The height was chosen both to give the electric fields in vacuum space to decay, and to match the height of the cavity in which the sample is to be placed. The lengths of the readout resonators $l$ were initially determined from $l = \frac{c}{2\sqrt{\varepsilon_{\text{eff}} f}}$, where $c$ is the speed of light, $\varepsilon_{\text{eff}}$ is the waveguide's effective dielectric constant [62, sec. 2.2], and $f$ is the resonance frequency. The relation between the resonator length and the simulated resonant frequency was then fit to the model

$$f = A/l + B, \tag{4.5}$$

where $A$ and $B$ are fitting parameters. The $A$ coefficient captures the inverse relation between resonator length and frequency. The offset term $B$ accounts for non-idealities including fringing fields. Coupling $Q$ factors were determined from the linewidth of the simulated transmission spectra, and confirmed by a three-port simulation of the couplers. Figure 4.3 shows the 2-port simulation of a $\lambda/2$ resonator, a three-port simulation of the coupler, and the transmission spectrum of the resonator. The coupling $Q$ is confirmed by the transmission spectrum in Figure 4.3 (c).

Having completed the simulations, design variations were then selected. The fabrication process accommodates $7 \times 3$ mm or $7 \times 7$ mm dies, each with up to eight RF connections on the chip. Four connections were required for these devices, two for the control lines, and two for the readout lines. This setup was chosen to match other experiments besides the CSFQ in the fabrication run, and reduce the amount of rewiring between cooldowns. The $7 \times 3$ mm dies were selected, owing to more dies being available for more qubits to be made. Up to four qubits could fit on each die, with most of the space taken up by $\lambda/2$ readout resonators. Figure 4.4 shows a CAD drawing of the baseline variation.

The baseline variation centered around an $I_c$ of 172 nA, and an $\alpha$ of 0.61. This was chosen to match the qubit on which qutrit RB was conducted. A variation involving a Purcell filter, and a variation with double the drive line coupling was also added. Variations sweeping $I_c$ from 112 to 212 nA, and sweeping $\alpha$ from 0.54 to 0.68 were added. Finally, the resonator Q of $85K$ was selected in addition to $170K$, in order to observe larger dispersive shifts and determine the impact of stronger resonator coupling on coherence.

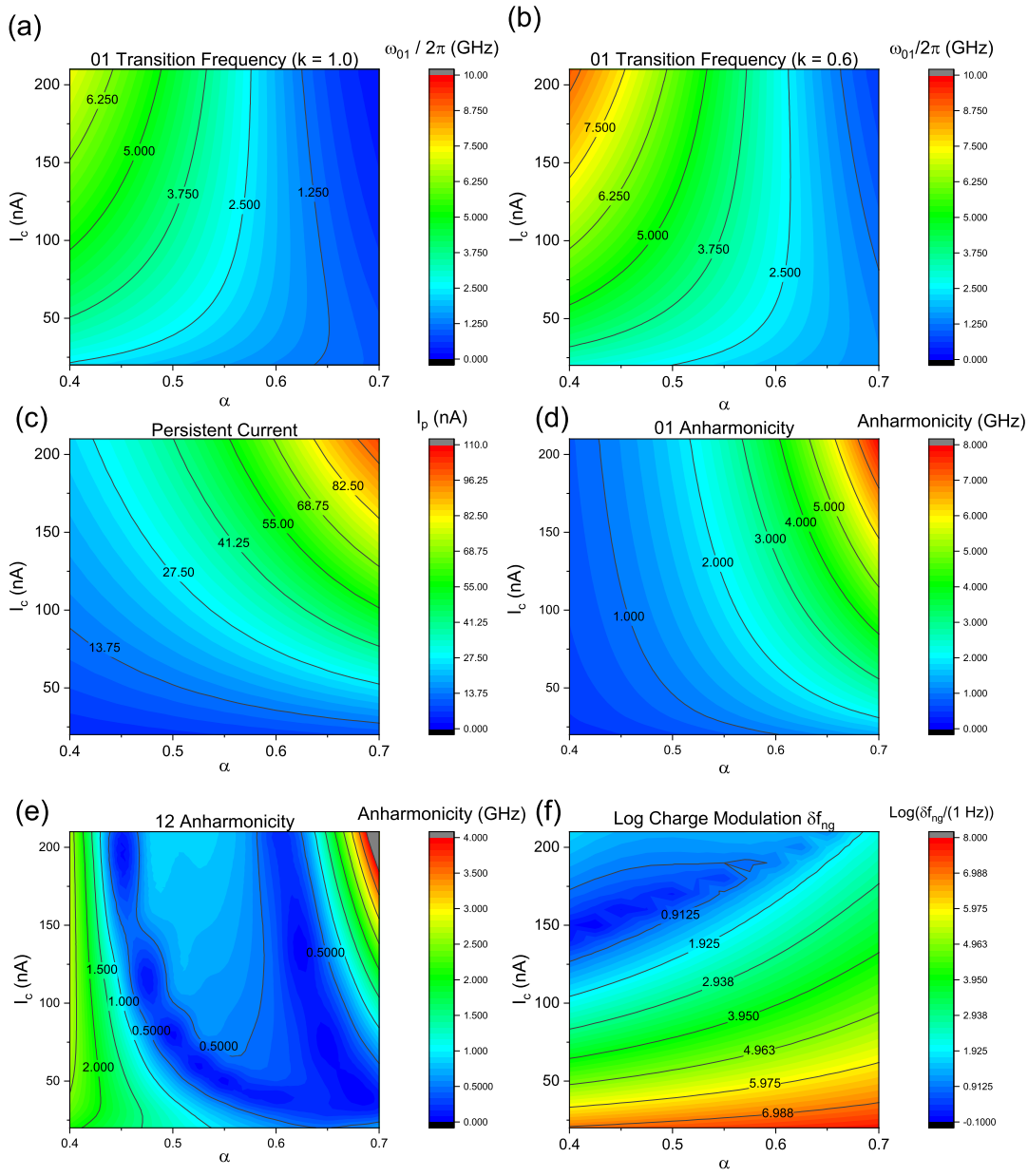


Figure 4.2: Plots of design parameters as a function of the critical current $I_c$ and $\alpha$. (a) The 01 transition frequency. (b) The 01-transition frequency with geometry scaled by 0.6. (c) The persistent current. (d) The 01 anharmonicity. (e) The difference betwen $\omega_{23}$ and $\omega_{12}$, and (f) the charge modulation.

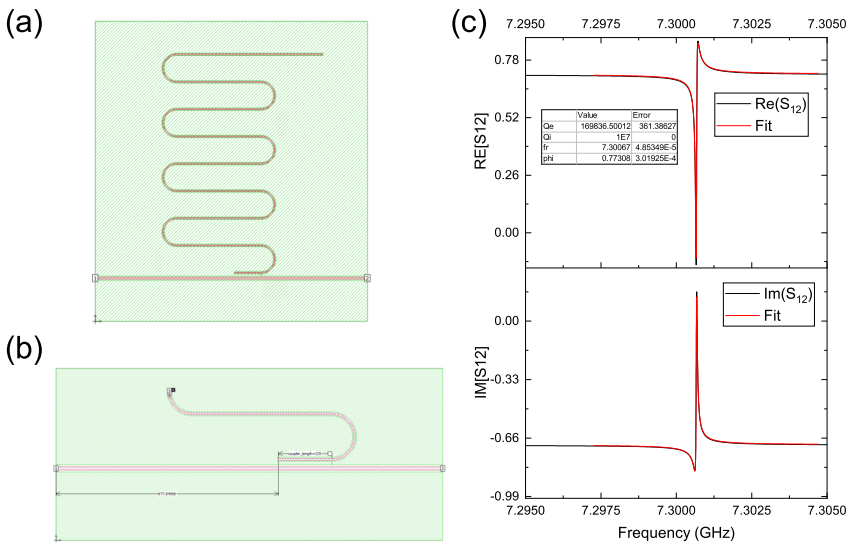


Figure 4.3: Simulation results of (a) a 7.3 GHz half-wavelength resonator coupled to a feedline, and (b) the portion of the resonator from (a) coupling to the feedline, with the other end connected to a 50 Ω port. (c) The real and imaginary components of $S_{12}$ obtained from the resonator in (a), with a simultaneous fit of the components to the expected $S_{12}$.

The qubits are fabricated using a planar process involving three layers, starting with a silicon wafer. The first layer etches cross-shaped markers 1.5 $\mu$m deep markers into the silicon. The second layer is a lift-off of 100 nm of Al evaporated onto the silicon. Optical lithography is used in this step to pattern large features down to a resolution of 2 $\mu$m. Aluminum is evaporated over three angles in order to get a stepped profile of Al, and so get good adhesion between the second and third layer of writing. The third layer consists of electron-beam lithography and shadow evaporation of Al onto the silicon. Electron beam lithography is used to pattern small features. The Josephson junctions are made by evaporating Al at one angle, oxidizing the Al, and then evaporating Al at the opposing angle [59]. Starting from a 4" wafer, the wafer is divided into 21 17$\times$17 mm (Approximately 1" diagonal) square chips, and the chips are further divided into either ten $7 \times 3$ mm dies. One die can be studied at a time in the cryostat.

The process imposes minimum dimensions on the required features. It is difficult to make a junction narrower than 65 nm, as the process introduces a 6 nm random error into junction dimensions. In addition, a 100 nm junction requires patterning a 50 nm wide feature into EBL resist, as the fabrication process results in junctions wider than the lithographically-defined size. The process sets a minimum variation of $I_c$ and $\alpha$, since a 10 nm random error in junction size can shift $\alpha$ by 0.05. This affects qubits in the high $I_c$ and low $\alpha$ region, requiring large variations in $\alpha$ in order to view systematic differences between qubits. The process also requires that no critical features are within 300 $\mu$m of the die, as this is where the ground plane is wirebonded to the device package. Finally, the process fixes the location of the microwave connectors on the die, as these need to be wirebonded to fixed traces on the package.

Figure 4.4 shows the baseline CAD design for the qubit. The readout resonators have a frequency of 7.1, 7.3, 7.5, and 7.7 GHz, respectively. All qubits except the last one have a critical current of 172 nA. The right-most qubit has an $I_c$ of 132 nA and the $\alpha$s are 0.61, 0.68, 0.54, and 0.61, looking from left to right.

## 4.3 Coupled CSFQ Devices

The single qubit CSFQ design work introduced in Section 4.2 furthers the understanding of varying design dimensions in the CSFQ sufficiently to consider two-qubit gates being applied on these devices. Two-qubit gates, like CNOT, SWAP, or CZ, are gates where the action on the target qubit depends on the state of a control qubit. It is impossible to construct a universal multi-qubit gate set without a two-qubit gate, but only one two-qubit gate is needed to realize a universal gate set [5, sec. 4.5.2].

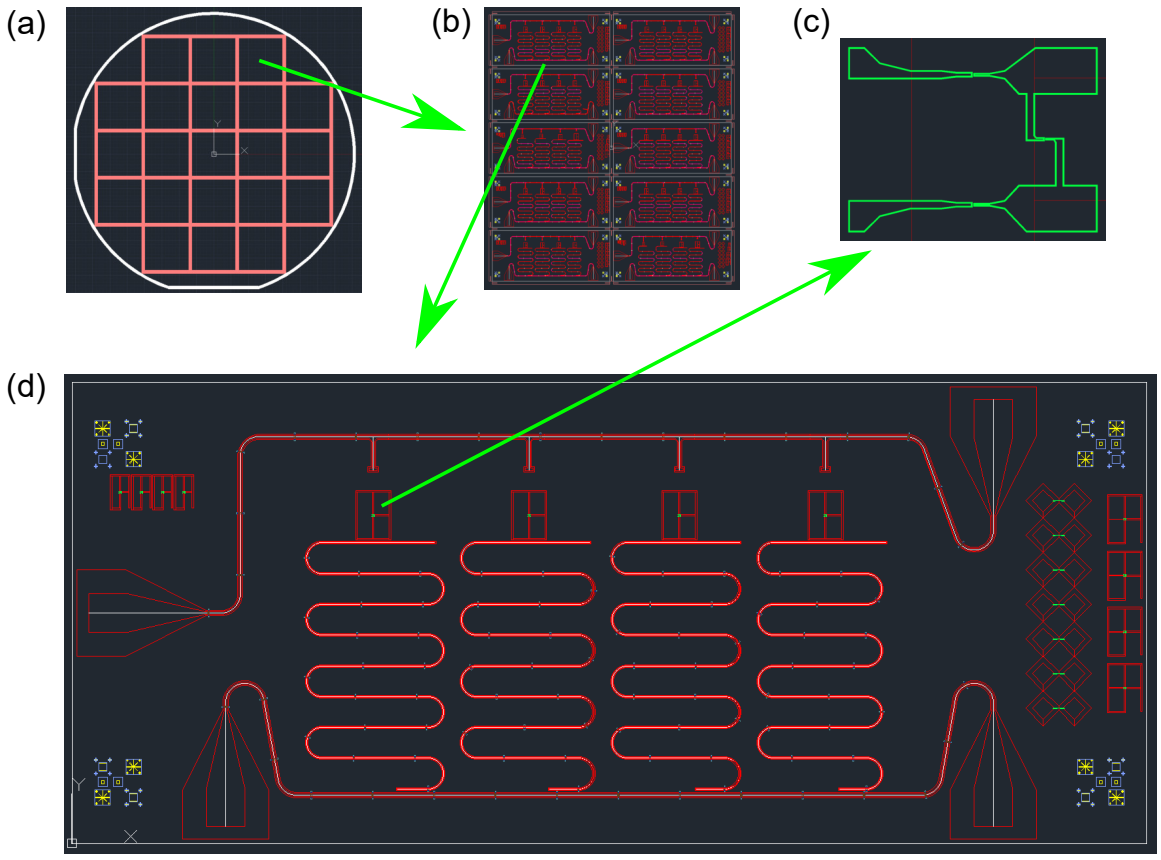


Figure 4.4: A drawing showing the baseline variation for the single-CSFQ device. (a) The partitioning of a 4" wafer into chips, and the location of the $17 \times 17$ mm chip on the wafer. (b) The $17 \times 17$ mm chip partitioned into $7 \times 3$ mm dies, and the location of the baseline variation on this chip. (c) The baseline variation of the Josephson junction for (d) the single-qubit CSFQ design. Green arrows indicate the direction in scaling, from large features to small features.

When considering the two-qubit design, there are further design attributes that need to be considered in addition to those in Section 4.2. The first such design parameter is the choice between inductive [63] or capacitive [52] coupling. Whereas inductive coupling is useful for tunable couplers, and generally implements a $\sigma_z \otimes \sigma_z$ interaction, the capacitive coupling implements transverse $\sigma_x \otimes \sigma_x$ and $\sigma_y \otimes \sigma_y$-type interactions. Pauli operators are written in the flux basis. Capacitive coupling was chosen since the small loops located at the center of large shunting pads would require cutting into the design to run inductors close enough to get good coupling.

The next parameter is the choice between fixed and tunable coupling. Fixed couplers offer fewer channels for decoherence, and are much simpler to design. However, the coupling cannot be switched off as in the case of a tunable coupler. The fixed coupling scheme was chosen, with the understanding that tunable couplers can be built using the information taken from a fixed coupling scheme.

The next design consideration is to consider what two-qubit gate to apply. For fixed coupling, the candidates are the selective darkening (SD) gate, the cross-resonance (CR) gate, and the frequency-tuned gate. The CR gate is the simplest type of two qubit gate, performed by driving the control qubit at the frequency of the target qubit. [64] Improvements to this gate by [65] include adding a drive to the target qubit, and then a correction pulse on the control qubit. The experiment described in [65] realized $\sigma_z \otimes \sigma_x$ gate to $99.1 \pm 0.2\,\%$ average gate fidelity (See section 2.6.1) in 160 ns with a 3.8 MHz qubit-qubit coupling. When the drive is stopped at the appropriate time, the drive realizes a CNOT gate. SD differs from the CR gate by driving the target qubit in addition to driving the control qubit. The extra tone in the SD gate suppresses the $|01\rangle - |11\rangle$ transition, in order to realize the a CNOT gate faster than the CR gate [66]. Both the SD and CR gates have been demonstrated to fidelity exceeding 99 %.

The frequency-tuned gate is also another route to a two-qubit gate. It works by tuning the qubits to the same resonant frequency, and then waiting for the coupling to produce a SWAP-type interaction between the qubits [67]. These gates are generally much faster than the SD and CR gates for a given coupling strength, but they require moving qubits away from the symmetry point, which reduces the coherence time. Recent work also outlines a method of suppressing the flux noise by incorporating AC drive and DC flux biasing to realize a two-qubit gate. [68]

Having outlined the approaches to produce a two-qubit gate, it is clear that the coupling strength must be determined to have an estimate of the gate time. This can be done by starting from the three-pad CSFQ Lagrangian, and adding terms corresponding to capacitances between the islands. The coupled qubit system goes from having two degrees

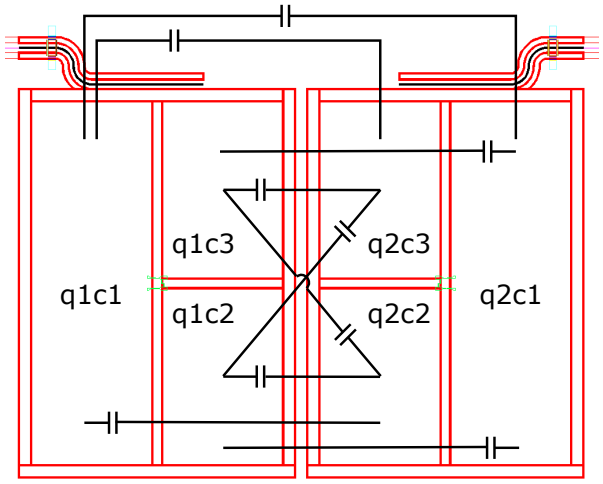


Figure 4.5: A drawing of the coupled CSFQ device, with coupling capacitances indicated. Each label refers to a pad on the CSFQ device, with each pad on the left qubit $Q1$ capacitively coupled to each pad on $Q2$.

of freedom to four degrees. Figure 4.5 shows a representation of the two-qubit coupled CSFQs, with additional coupling capacitances indicated.

To determine the coupling strength, begin with the capacitance matrix $C_{ij}$ as shown in equation 2.16 of Section 2.1, which incorporates the coupling terms. The terms coupling $n$ operators on qubits 1 and 2 can be separated, such that $C^{-1} = C_1^{-1} + C_2^{-1} + C_{int}^{-1}$. $C_1^{-1}$ is a block-diagonal matrix containing only elements in the upper-left 2x2 block of the 4 x 4 coupling matrix, $C_2^{-1}$ is block-diagonal in the lower-right 2x2 block, and $C_{int}^{-1}$ contains the off-diagonal element. The interaction Hamiltonian then has the form

$$H_{\text{int}} = \frac{\hbar^2}{2} \begin{pmatrix} n_{1,1} & n_{1,2} & n_{2,1} & n_{2,2} \end{pmatrix} C_{int}^{-1} \begin{pmatrix} n_{1,1} \\ n_{1,2} \\ n_{2,1} \\ n_{2,2} \end{pmatrix}, \tag{4.6}$$

where $n_{k,m}$ is the $m$ number operator on qubit $k$. The coupling strength $g_{01}$ can then be determined by taking the matrix element $\langle 01|H_{\text{int}}|10\rangle$. Coupling strengths can be determined this way for higher levels as well. To consider the coupling strength for $\sigma_x \otimes \sigma_x$ or $\sigma_y \otimes \sigma_y$ interactions, this coupling strength $g$ can be obtained through

$$g = \text{tr}\left((\sigma_x \otimes \sigma_x) H_{\text{int}}\right). \tag{4.7}$$

A large coupling strength is desirable to speed up the two-qubit gate. However, the coupling must also be much less than the detuning between the qubits for the SD gate to function. In addition, the treatment of the coupling constant presented here presents the coupling as a perturbation to the individual qubit states. If the qubits couple strongly, then the eigenstates identified for the single qubit device will evolve too quickly in time to be prepared or read out.

In addition to the coupling strength, the qubits themselves must be selected to avoid collisions between certain frequencies. Firstly, the qubits must be detuned at their symmetry point to reduce crosstalk between control on the two qubits. However, if the detuning is too large, then SD will require a very large amplitude difference to implement the gate. For qubits $A$ and $B$ coupled with a strength of $g$, the ratio

$$\frac{|\omega_{01,A} - \omega_{01,B}|}{g} \tag{4.8}$$

should be between 3 and 10. The lower bound exists so that the control and target qubit can be distinguished in the device, and the upper bound exists so that the amplitude ratio between the control and target drive in the SD gate is not too large, and thus difficult to experimentally realize.

The other collision criteria involve the transition frequencies for the 01 and 12 transitions, as well as the 02 two-photon transitions. These should be well-separated for the two qubits to ensure that they can be addressed independently. Given fabrication uncertainties, it is best for these transitions to be separated by at least 100 MHz.

Having discussed the parameters for the design, we now discuss the dimensions that can be varied in the design. To keep the design symmetric, it was decided to keep the scale factor common to both qubits, and rely on variations in junction design to change the transition frequencies. In addition to $k = 1.0$ for the baseline qubit, a high-frequency qubit with $k = 0.6$ was used to increase the transition frequency, and counteract the transition frequency drop expected with adding additional capacitances to the individual qubits. $k = 0.8$ was also chosen as a compromise scale factor between the two extremes.

The coupling strength was adjusted by increasing the spacing between the two qubits. At a minimum distance of 10 $\mu$m between the qubits, $g = 40$ MHz. A piece of the ground plane was kept between the qubits to avoid opening a large hole in the ground plane, and reducing coherence. The width of this piece of ground plane sets the minimum distance between the qubits, and was set to match the width of the gaps between CSFQ plates. This way, the ground plane around each qubit is closed.

Finally, the design of the flux biasing on chip needs to be considered. Whereas the single-qubit devices rely on a global magnetic field for the flux bias, the coupled qubits are

too close together to bias the coupled qubits independently, as this would require a large magnetic field gradient to be produced. Therefore, a local flux bias needs to be applied to each qubit. This was accomplished by placing a transmission line near the qubit and shorting it to the ground plane. Relevant dimensions include the distance of the flux line from the qubit, and the length of the line. Having the flux line close to the qubit loop increases the inductance, and so reduces the current required to bias the qubit. However, the extra inductance also makes the qubit more susceptible to flux noise. The goal of keeping a closed ground plane around the CSFQ also conflicts with having a thin section of ground plane near a flux line, as this offers a return path for the bias current, reducing the effectiveness of the line.

To evaluate the inductance of the flux line, the inductance was calculated using FastHenry. The central trace and gap on the flux line are the same size as the readout resonators, in order to match the transmission line to 50 Ω. An S-turn was added to put a section of ground plane at the corner of the qubit. From the FastHenry simulation, the mutual inductance between the flux line and the qubit loop is 0.48 pH. This means that 4.23 $\mu$A will be needed to add a flux of 1 m$\Phi_0$ to the qubit. This is sufficient for fine tuning. The worst-case loss through the flux line $\Gamma$ is determined by

$$\Gamma = \frac{\omega_{01}}{\pi} \left( \frac{M I_p}{\phi_0} \right)^2 \frac{R_Q}{Z_0} \tag{4.9}$$

where $M$ is the mutual inductance, $I_p$ is the persistent current, $\phi_0$ is the flux quantum, $R_Q = 6.4\,\mathrm{k}\Omega$ is the resistance quantum, and $Z_0$ is the impedance of the line. This gives $\Gamma = 3.1$ KHz, which is much smaller than $\Gamma$ through other noise sources.

With these design considerations in mind, Figure 4.6 shows the baseline variation of the coupled qubit device. The frequency of the readout resonators are 7.3 and 7.5 GHz, respectively. The critical currents are 172 nA and 132 nA, and the respective alphas are 0.60 and 0.62. The detuning is 6.14 times larger than the coupling strength of 40.2 MHz, and the closest frequency collision of 270 MHz occurs between the $1-2$ transition on qubit 1, and the $2-3$ transition on qubit 2. Variations on this device include qubits with a 2 GHz transition frequency with $k = 0.8$, and 4 GHz transition frequency with $k = 0.6$. The rationale for the 4 GHz devices was to raise the transition frequency as high as possible, sacrificing anharmonicity for low ground state population, and faster two-qubit gate performance. Features on the flux line include a tapered connector to keep the line at 50 Ω impedance, and rounded corners ensure reliable transmission up to RF range. This enables the flux bias to be altered during an experiment, on the timescale of qubit transitions.

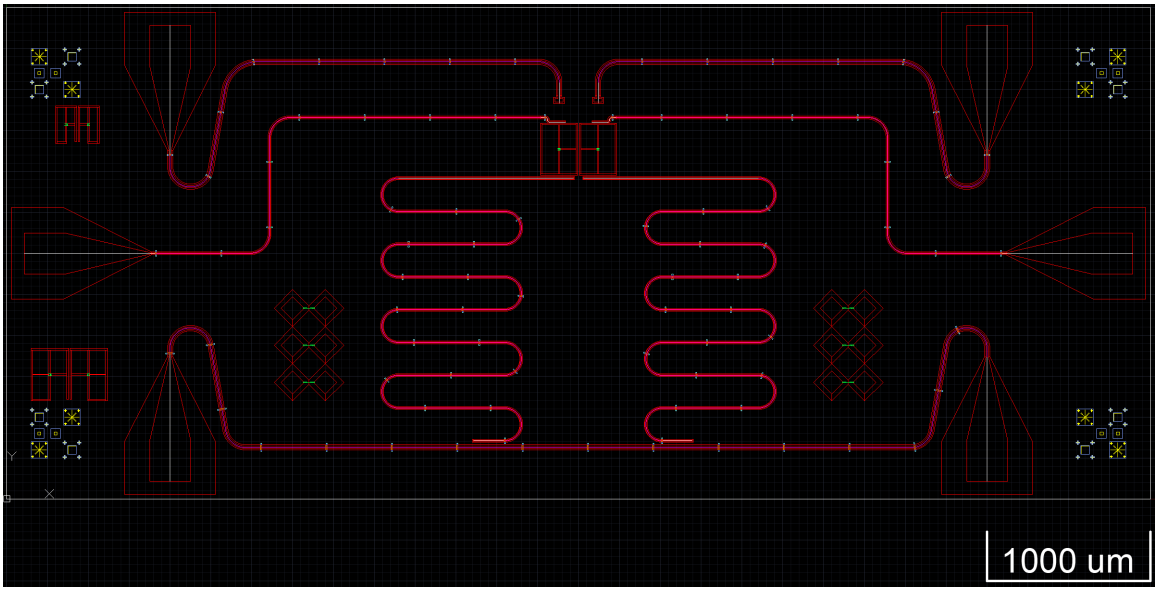


Figure 4.6: A drawing of the baseline variation of the coupled CSFQ device. The two qubits to be coupled are in the center of the device. Each qubit has a dedicated readout resonator, control line, and flux line. Test structures are placed on the chip to check junction critical current, and the quality of lithography. Alignment marks (blue and yellow structures) are placed in the corners to ensure dimensional alignment during lithography.

## 4.4 Conclusions

With the single qubit devices from Section 4.2, and the two-qubit devices from Section 4.3, progress has been made toward the goal of producing a two-qubit gate with new CSFQs. To do this, the design goals were considered against a desirable set of parameters for the qubit, and the design dimensions were varied to understand their impact on the design parameters. Simulations helped to map the dimensions to design parameters, and variations were selected for the single-qubit device. Some modeling was done on the coupling for the coupled CSFQ device, and variations were selected in this device as well. The product is a set of devices ready to be manufactured and studied experimentally.

The challenges in these designs were effectively filling the frequency spectrum, having to design to a fabrication process, and determining coupling strengths between the qubits and control lines. For filling the frequency spectrum, it was important to make sure that each transition can be driven effectively, and to leave enough space between transitions so that they are well-separated. This challenge was compounded by having multiple qubits on a single chip, and by having to leave large gaps in the spectrum to account for fabrication uncertainties. As more devices are added, the collision conditions will become stricter, requiring more information to be known about variations in the CSFQ, and tighter control over fabrication. This motivates the single-qubit design study, just as determining the coupling strength and determining two-qubit gate strategies for coupled CSFQs motivates the need for the two-qubit devices.

Nevertheless, the designs selected show promise as they are built on a proven CSFQ design, on which high-fidelity qutrit control was demonstrated. This validates the model for these devices, and paves the way for research into multi-qudit devices. The selective darkening and cross-resonance gate techniques are also established, and give proven strategies for implementing two-qubit gates. It is expected that the high anharmonicity persists into this new round of devices, and the coherence time is to be retained. These features will yield high-fidelity two-qubit gates.

The next steps for this design include manufacture, device characterization, and experimentation. Test structures will be used in the fabrication run to determine the critical current density, which will inform the corrections to the junction parameters. After this is information is included into the design, and new devices are manufactured, the next step will be spectroscopy experiments on single-qubit devices to determine transition frequencies and anharmonicities. Rabi experiments will then establish the control parameters, and coherence experiments including Ramsey interferometry will give the $T_1$ and pure dephasing rates. Cooling experiments will then be conducted to improve state preparation, and

RB experiments will be used to characterize control on single-qubit devices. All this will then be repeated on a separate cooldown with two-qubit devices, leading to two-qubit gate experiments.

# Chapter 5

# Conclusions

This thesis presented a qutrit randomized benchmarking experiment in Chapter 3, showing that high-fidelity qutrit control can be performed on a three-pad capacitively-shunted flux qubit. The experiment identified level shift correction and leakage suppression as future directions for improving qutrit gate fidelity. Combined with the understanding of flux qubits presented in Chapter 2, this motivated a new set of CSFQ devices to be designed. Chapter 4 presented a single-qubit device on which control can be improved, as well as a device for studying two-qubit gates. Candidates for two-qubit gates have been proposed.

From the qutrit RB experiment in Chapter 3, it was concluded that level shifts due to off-resonant coupling to states outside the two-dimensional subspace of a Givens rotation were responsible for most of the error. Leakage outside the qutrit space, and decoherence also contributed to the experiment error. Nevertheless, the control scheme was capable of synthesizing the qutrit Clifford group to an average fidelity of 99%, motivating further development of qutrit control in this device.

From the design study in Chapter 4, a set of multiplexed one-qubit and a set of two-qubit devices were produced, which are ready for fabrication. The CSFQ model presented in Chapter 2, and confirmed by experiment in [10] and [11] was applied to a broad space of possible qubit designs, and new qubit designs were selected based on this study. The coupling strength between two CSFQs was also estimated, and used to inform device designs to study two-qubit gates. The presented designs are ready for fabrication and testing.

In summary, the three-pad CSFQ device has performed well so far as a candidate device for building a quantum computer. Single-qubit preparation, control, and readout

have been demonstrated, as well as high-fidelity qutrit control. The next step is to understand how multiple three-pad CSFQs couple together, and how to perform two-qubit gates experimentally.

Future work on the CSFQ includes fabrication and study of single-qubit devices of the type presented in Section 4.2. These devices are good test beds for varying junctions and capacitive pad geometries to further improve coherence and quantum control. They are also good test beds for studying single-qubit control. Variations on RB such as interleaved RB and leakage RB can be used to identify different types of gate errors. New gate decompositions, possibly extending [11], can then be tested, in order to find new qudit control schemes for CSFQs. This work can then be taken to two-qubit devices to obtain high-fidelity two-qubit gates, and so realize universal gate sets for quantum computing. The next step will then be to integrate many CSFQs together, and compute on these many-CSFQ devices.

# References


[1] M. Kononenko, M. A. Yurtalan, J. Shi, and A. Lupascu, "Characterization of Control in a Superconducting Qutrit Using Randomized Benchmarking," *arXiv:2009.00599 [quant-ph]*, Sept. 2020.

[2] R. Barends, J. Kelly, A. Megrant, D. Sank, E. Jeffrey, *et al.*, "Coherent Josephson Qubit Suitable for Scalable Quantum Integrated Circuits," *Physical Review Letters*, vol. 111, p. 080502, Aug. 2013.

[3] C. J. Wood and J. M. Gambetta, "Quantification and Characterization of Leakage Errors," *Physical Review A*, vol. 97, p. 032306, Mar. 2018.

[4] A. Montanaro, "Quantum algorithms: An overview," *npj Quantum Information*, vol. 2, pp. 1–8, Jan. 2016.

[5] M. A. Nielsen and I. L. Chuang, *Quantum Computation and Quantum Information*. Cambridge: Cambridge University Press, first south asia edition ed., 2013.

[6] J. Helsen, I. Roth, E. Onorati, A. H. Werner, and J. Eisert, "A general framework for randomized benchmarking," *arXiv:2010.07974 [quant-ph]*, Oct. 2020.

[7] M. Kjaergaard, M. E. Schwartz, J. Braumüller, P. Krantz, J. I.-J. Wang, S. Gustavsson, and W. D. Oliver, "Superconducting Qubits: Current State of Play," *Annual Review of Condensed Matter Physics*, vol. 11, pp. 369–395, Mar. 2020.

[8] M. A. Yurtalan, *Multi-Level Control in Large-Anharmonicity High-Coherence Capacitively Shunted Flux Quantum Circuits*. PhD thesis, University of Waterloo, Apr. 2019.

[9] T. P. Orlando, J. E. Mooij, L. Tian, C. H. van der Wal, L. S. Levitov, *et al.*, "Superconducting persistent-current qubit," *Physical Review B*, vol. 60, pp. 15398–15413, Dec. 1999.

[10] M. A. Yurtalan, J. Shi, G. J. K. Flatt, and A. Lupascu, "Characterization of multilevel dynamics and decoherence in a high-anharmonicity capacitively shunted flux circuit," *arXiv:2008.00593 [quant-ph]*, Aug. 2020.

[11] M. A. Yurtalan, J. Shi, M. Kononenko, A. Lupascu, and S. Ashhab, "Implementation of a Walsh-Hadamard Gate in a Superconducting Qutrit," *Physical Review Letters*, vol. 125, p. 180504, Oct. 2020.

[12] J. Bardeen, L. N. Cooper, and J. R. Schrieffer, "Theory of Superconductivity," *Physical Review*, vol. 108, pp. 1175–1204, Dec. 1957.

[13] I. Askerzade, A. Bozbey, and M. Cantürk, *Modern Aspects of Josephson Dynamics and Superconductivity Electronics*. Mathematical Engineering, Cham: Springer International Publishing : Imprint: Springer, 1st ed. 2017 ed., 2017.

[14] G. Burkard, R. H. Koch, and D. P. DiVincenzo, "Multilevel quantum description of decoherence in superconducting qubits," *Physical Review B*, vol. 69, p. 064503, Feb. 2004.

[15] U. Vool and M. Devoret, "Introduction to quantum electromagnetic circuits," *International Journal of Circuit Theory and Applications*, vol. 45, no. 7, pp. 897–934, 2017.

[16] Y. Nakamura, Y. A. Pashkin, and J. S. Tsai, "Coherent control of macroscopic quantum states in a single-Cooper-pair box," *Nature*, vol. 398, pp. 786–788, Apr. 1999.

[17] J. J. Sakurai and S. F. Tuan, *Modern Quantum Mechanics*. Reading, Mass: Addison-Wesley Pub. Co, rev. ed ed., 1994.

[18] J. Koch, T. M. Yu, J. Gambetta, A. A. Houck, D. I. Schuster, J. Majer, A. Blais, M. H. Devoret, S. M. Girvin, and R. J. Schoelkopf, "Charge-insensitive qubit design derived from the Cooper pair box," *Physical Review A*, vol. 76, p. 042319, Oct. 2007.

[19] A. Lupaşcu, P. Bertet, E. F. C. Driessen, C. J. P. M. Harmans, and J. E. Mooij, "One- and two-photon spectroscopy of a flux qubit coupled to a microscopic defect," *Physical Review B*, vol. 80, p. 172506, Nov. 2009.

[20] E. Jeffrey, D. Sank, J. Y. Mutus, T. C. White, J. Kelly, *et al.*, "Fast Accurate State Measurement with Superconducting Qubits," *Physical Review Letters*, vol. 112, p. 190504, May 2014.

[21] M. Boissonneault, J. M. Gambetta, and A. Blais, "Dispersive regime of circuit QED: Photon-dependent qubit dephasing and relaxation rates," *Physical Review A*, vol. 79, p. 013819, Jan. 2009.

[22] G. Ithier, E. Collin, P. Joyez, P. J. Meeson, D. Vion, *et al.*, "Decoherence in a superconducting quantum bit circuit," *Physical Review B*, vol. 72, p. 134519, Oct. 2005.

[23] P. Krantz, M. Kjaergaard, F. Yan, T. P. Orlando, S. Gustavsson, and W. D. Oliver, "A quantum engineer's guide to superconducting qubits," *Applied Physics Reviews*, vol. 6, p. 021318, June 2019.

[24] M. H. Levitt, *Spin Dynamics: Basics of Nuclear Magnetic Resonance*. Chichester, England ; Hoboken, NJ: Wiley, 2 edition ed., Apr. 2008.

[25] S. M. Anton, J. S. Birenbaum, S. R. O'Kelley, V. Bolkhovsky, D. A. Braje, *et al.*, "Magnetic Flux Noise in dc SQUIDs: Temperature and Geometry Dependence," *Physical Review Letters*, vol. 110, p. 147002, Apr. 2013.

[26] M.-D. Choi, "Completely positive linear maps on complex matrices," *Linear Algebra and its Applications*, vol. 10, pp. 285–290, June 1975.

[27] E. Magesan, J. M. Gambetta, and J. Emerson, "Scalable and Robust Randomized Benchmarking of Quantum Processes," *Physical Review Letters*, vol. 106, p. 180504, May 2011.

[28] M. A. Nielsen, "A simple formula for the average gate fidelity of a quantum dynamical operation," *Physics Letters A*, vol. 303, pp. 249–252, Oct. 2002.

[29] J. Emerson, R. Alicki, and K. \.Zyczkowski, "Scalable noise estimation with random unitary operators," *Journal of Optics B: Quantum and Semiclassical Optics*, vol. 7, pp. S347–S352, Sept. 2005.

[30] I. L. Chuang and M. A. Nielsen, "Prescription for experimental determination of the dynamics of a quantum black box," *Journal of Modern Optics*, vol. 44, pp. 2455–2467, Nov. 1997.

[31] E. Magesan, J. M. Gambetta, B. R. Johnson, C. A. Ryan, J. M. Chow, *et al.*, "Efficient measurement of quantum gate error by interleaved randomized benchmarking," *Physical Review Letters*, vol. 109, p. 080505, Aug. 2012.

[32] F. Arute, K. Arya, R. Babbush, D. Bacon, J. C. Bardin, *et al.*, "Quantum supremacy using a programmable superconducting processor," *Nature*, vol. 574, pp. 505–510, Oct. 2019.

[33] J. S. Otterbach, R. Manenti, N. Alidoust, A. Bestwick, M. Block, *et al.*, "Unsupervised Machine Learning on a Hybrid Quantum Computer," *arXiv:1712.05771 [quant-ph]*, Dec. 2017.

[34] A. D. Corcoles, A. Kandala, A. Javadi-Abhari, D. T. McClure, A. W. Cross, K. Temme, P. D. Nation, M. Steffen, and J. M. Gambetta, "Challenges and Opportunities of Near-Term Quantum Computing Systems," *arXiv:1910.02894 [quant-ph]*, Oct. 2019.

[35] K. Wright, K. M. Beck, S. Debnath, J. M. Amini, Y. Nam, *et al.*, "Benchmarking an 11-qubit quantum computer," *Nature Communications*, vol. 10, p. 5464, Nov. 2019.

[36] E. T. Campbell, "Enhanced Fault-Tolerant Quantum Computing in $d$-Level Systems," *Physical Review Letters*, vol. 113, p. 230501, Dec. 2014.

[37] E. T. Campbell, H. Anwar, and D. E. Browne, "Magic-State Distillation in All Prime Dimensions Using Quantum Reed-Muller Codes," *Physical Review X*, vol. 2, p. 041021, Dec. 2012.

[38] H. Anwar, B. J. Brown, E. T. Campbell, and D. E. Browne, "Fast decoders for qudit topological codes," *New Journal of Physics*, vol. 16, p. 063038, June 2014.

[39] A. Krishna and J.-P. Tillich, "Towards Low Overhead Magic State Distillation," *Physical Review Letters*, vol. 123, p. 070507, Aug. 2019.

[40] A. R. Shlyakhov, V. V. Zemlyanov, M. V. Suslov, A. V. Lebedev, G. S. Paraoanu, *et al.*, "Quantum metrology with a transmon qutrit," *Physical Review A*, vol. 97, p. 022115, Feb. 2018.

[41] M. V. Suslov, G. B. Lesovik, and G. Blatter, "Quantum abacus for counting and factorizing numbers," *Physical Review A*, vol. 83, p. 052317, May 2011.

[42] F. Bouchard, R. Fickler, R. W. Boyd, and E. Karimi, "High-dimensional quantum cloning and applications to quantum hacking," *Science Advances*, vol. 3, p. e1601915, Feb. 2017.

[43] C. M. Dawson and M. A. Nielsen, "The Solovay-Kitaev algorithm," *Quantum Information & Computation*, vol. 6, pp. 81–95, Jan. 2006.

[44] S. G. Schirmer, A. D. Greentree, V. Ramakrishna, and H. Rabitz, "Constructive control of quantum systems using factorization of unitary operators," *Journal of Physics A: Mathematical and General*, vol. 35, pp. 8315–8339, Sept. 2002.

[45] A. N. Glaudell, N. J. Ross, and J. M. Taylor, "Canonical forms for single-qutrit Clifford+T operators," *Annals of Physics*, vol. 406, pp. 54–70, July 2019.

[46] M. Jafarzadeh, Y.-D. Wu, Y. R. Sanders, and B. C. Sanders, "Randomized benchmarking for qudit Clifford gates," *New Journal of Physics*, vol. 22, p. 063014, June 2020.

[47] D. Gottesman, "Fault-Tolerant Quantum Computation with Higher-Dimensional Systems," in *Quantum Computing and Quantum Communications* (C. P. Williams, ed.), Lecture Notes in Computer Science, (Berlin, Heidelberg), pp. 302–313, Springer, 1999.

[48] J. R. Johansson, P. D. Nation, and F. Nori, "QuTiP 2: A Python framework for the dynamics of open quantum systems," *Computer Physics Communications*, vol. 184, pp. 1234–1240, Apr. 2013.

[49] R. A. Bertlmann and P. Krammer, "Bloch vectors for qudits," *Journal of Physics A: Mathematical and Theoretical*, vol. 41, p. 235303, May 2008.

[50] L. B. Nguyen, Y.-H. Lin, A. Somoroff, R. Mencia, N. Grabon, and V. E. Manucharyan, "High-Coherence Fluxonium Qubit," *Physical Review X*, vol. 9, p. 041041, Nov. 2019.

[51] J. Bylander, S. Gustavsson, F. Yan, F. Yoshihara, K. Harrabi, *et al.*, "Dynamical decoupling and noise spectroscopy with a superconducting flux qubit," *Nature Physics*, vol. 7, pp. 565–570, July 2011.

[52] X. Li, Y. Ma, J. Han, T. Chen, Y. Xu, *et al.*, "Perfect Quantum State Transfer in a Superconducting Qubit Chain with Parametrically Tunable Couplings," *Physical Review Applied*, vol. 10, p. 054009, Nov. 2018.

[53] F. Motzoi, J. M. Gambetta, P. Rebentrost, and F. K. Wilhelm, "Simple Pulses for Elimination of Leakage in Weakly Nonlinear Qubits," *Physical Review Letters*, vol. 103, p. 110501, Sept. 2009.

[54] Y. Makhlin and A. Shnirman, "Dephasing of Solid-State Qubits at Optimal Points," *Physical Review Letters*, vol. 92, p. 178301, Apr. 2004.

[55] D. S. Holmes and J. McHenry, "Non-normal Critical Current Distributions in Josephson Junctions With Aluminum Oxide Barriers," *IEEE Transactions on Applied Superconductivity*, vol. 27, pp. 1–5, June 2017.

[56] M. A. Sulangi, T. A. Weingartner, N. Pokhrel, E. Patrick, M. Law, *et al.*, "Disorder and critical current variability in Josephson junctions," *Journal of Applied Physics*, vol. 127, p. 033901, Jan. 2020.

[57] N. T. Bronn, E. Magesan, N. A. Masluk, J. M. Chow, J. M. Gambetta, and M. Steffen, "Reducing Spontaneous Emission in Circuit Quantum Electrodynamics by a Combined Readout/Filter Technique," *IEEE Transactions on Applied Superconductivity*, vol. 25, pp. 1–10, Oct. 2015.

[58] C. Wang, C. Axline, Y. Y. Gao, T. Brecht, Y. Chu, *et al.*, "Surface participation and dielectric loss in superconducting qubits," *Applied Physics Letters*, vol. 107, p. 162601, Oct. 2015.

[59] G. J. Dolan, "Offset masks for lift-off photoprocessing," *Applied Physics Letters*, vol. 31, pp. 337–339, Sept. 1977.

[60] D. M. Pozar, *Microwave Engineering*. Hoboken, NJ: Wiley, 4th ed ed., 2012.

[61] J. Braumüller, L. Ding, A. P. Vepsäläinen, Y. Sung, M. Kjaergaard, *et al.*, "Characterizing and Optimizing Qubit Coherence Based on SQUID Geometry," *Physical Review Applied*, vol. 13, p. 054079, May 2020.

[62] R. Simons, *Coplanar Waveguide Circuits, Components, and Systems*. Wiley Series in Microwave and Optical Engineering, New York: John Wiley, 2001.

[63] D. Kafri, C. Quintana, Y. Chen, A. Shabani, J. M. Martinis, and H. Neven, "Tunable inductive coupling of superconducting qubits in the strongly nonlinear regime," *Physical Review A*, vol. 95, p. 052333, May 2017.

[64] C. Rigetti and M. Devoret, "Fully microwave-tunable universal gates in superconducting qubits with linear couplings and fixed transition frequencies," *Physical Review B*, vol. 81, p. 134507, Apr. 2010.

[65] S. Sheldon, E. Magesan, J. M. Chow, and J. M. Gambetta, "Procedure for systematically tuning up cross-talk in the cross-resonance gate," *Physical Review A*, vol. 93, p. 060302, June 2016.

[66] P. C. de Groot, J. Lisenfeld, R. N. Schouten, S. Ashhab, A. Lupaşcu, C. J. P. M. Harmans, and J. E. Mooij, "Selective darkening of degenerate transitions demonstrated with two superconducting quantum bits," *Nature Physics*, vol. 6, pp. 763–766, Oct. 2010.

[67] L. DiCarlo, J. M. Chow, J. M. Gambetta, L. S. Bishop, B. R. Johnson, *et al.*, "Demonstration of two-qubit algorithms with a superconducting quantum processor," *Nature*, vol. 460, pp. 240–244, July 2009.

[68] S. S. Hong, A. T. Papageorge, P. Sivarajah, G. Crossman, N. Didier, *et al.*, "Demonstration of a parametrically activated entangling gate protected from flux noise," *Physical Review A*, vol. 101, p. 012302, Jan. 2020.

# APPENDICES

# Appendix A

# Numerical Simulations of Density Matrix Evolution

The state of the circuit can be associated with a density operator $\rho$ representing a classical mixture of quantum states. For an ensemble with probabilities $p(\psi_i)$ of being in the state $|\psi_i\rangle$, the density operator is

$$\rho = \sum_i p(\psi_i) \, |\psi_i\rangle\langle\psi_i| \tag{A.1}$$

The time evolution of $\rho$ is given by the master equation

$$\dot{\rho} = \frac{i}{\hbar}[\rho, H] + L_i \rho L_i^\dagger - \frac{1}{2}\left\{L_i^\dagger L_i, \rho\right\} \tag{A.2}$$

where $H$ is the Hamiltonian. $L_i$ are the collapse operators of the system, which describe memoryless relaxation processes such as ohmic dissipation in resistors. To solve equation 2.26 numerically, express the density operator $\rho$ as a vector $|\rho\rangle$ using the column-stacking convention

$$\sum_{ij} \rho_{ij} \, |i\rangle\langle j| \rightarrow \sum_{ij} \rho_{ij} \, |i\rangle \, |j\rangle \, . \tag{A.3}$$

Left multiplication of $\rho$ by an operator $A$ transforms as

$$A\rho \rightarrow (A \otimes I) \, |\rho\rangle \tag{A.4}$$

where $I$ is the identity operator of the same dimension as $A$. Right multiplication of $\rho$ by an operator $B$ transforms as

$$\rho B \rightarrow (I \otimes B^T) \, |\rho\rangle \, , \tag{A.5}$$

and so the master equation becomes

$$|\dot{\rho}\rangle = \left( \left( -\frac{1}{2} L_i^\dagger L_i + \frac{i}{\hbar} H \right) \otimes I + I \otimes \left( -\frac{1}{2} L_i^\dagger L_i - \frac{i}{\hbar} H \right)^T + L_i \otimes (L_i^\dagger)^T \right) |\rho\rangle \,. \tag{A.6}$$

This master equation is of the form $\dot{y(t)} = Hy(t)$. Combined with initial conditions, this initial value problem can be solved by any ordinary differential equation solver.